

Computational Simulations of a non-Body of Revolution Ellipsoidal Model Utilizing
RANS

John Ryan Somero

Thesis submitted to the faculty of the Virginia Polytechnic Institute and State University
in partial fulfillment of the requirements for the degree of

Master of Science
In
Aerospace Engineering

Roger L. Simpson
Christopher J. Roy
Bernard M. Grossman

6 August, 2010
Blacksburg, VA

Keywords:

Ellipsoid, Computational Fluid Dynamics, Reynolds Averaged Navier-Stokes,
Maneuvering, Skin Friction

Computational Simulations of a non-Body of Revolution Ellipsoidal Model Utilizing RANS
John Ryan Somero

ABSTRACT

The ability of Reynolds Averaged Navier Stokes (RANS) models to predict the characteristics of a non-Body of Revolution (non-BOR) Ellipsoidal model is studied to establish the feasibility of utilizing RANS as a non-BOR concept design tool. Data unable to be obtained experimentally, such as streamwise and spanwise pressure gradients and yaw turn boundary layer characteristics, are also established. A range of conditions are studied including ahead, pitched up, steady 10 and 15 degree yaw turns, and unsteady 10 and 15 degree yaw turns. Simulation results show good agreement for ahead and pitched forces and moments. Straight ahead skin friction values also showed good agreement, providing even improved agreement over an LES model which utilized wall functions. Yaw turn conditions also showed good agreement for roll angles up to 10 degrees. Steady maneuvering forces and moments showed good agreement up to 10 degrees roll and separation calculations also showed good agreement up to 10 degrees roll. Unsteady maneuvering characteristics showed mixed results, with the normal force and pitching moment trends generally agreeing with experimental data, whereas the unsteady rolling moment did not tend to follow experimental trends. Two primary conditions, the change in curvature between the mid-body and elliptical ends and the accuracy of modeling of 3D flows with RANS, are discussed as sources of discrepancies between the experimental data and steady simulations greater than 10 degrees roll and unsteady rolling simulations.

Table of Contents

List of Figures	iv
List of Tables.....	v
I. Introduction	1
II. Literature Review	2
III. Simulation Approach.....	4
A. Simulation Code	4
B. Turbulence Models	4
C. Model Geometry.....	4
D. Computational Grids	5
E. Boundary Conditions.....	7
F. Model Uncertainties	8
1. Iterative Uncertainty.....	8
2. Grid Uncertainty	8
IV. Calculation Methods	10
A. Velocity	10
B. Pressure Coefficient.....	10
C. Wall Shear Stress.....	11
D. Ludwig-Tillman Shear Stress	11
E. Vorticity Flux	11
F. Maneuvering Characteristics	12
V. Results and Discussion	13
A. Steady Ahead.....	13
1. Straight Ahead Drag.....	13
2. Steady 10 Degree Angle of Attack.....	13
3. Straight Ahead Skin Friction.....	15
4. Straight Ahead Pressure Distributions	20
B. Steady Maneuvering	21
1. Steady Maneuvering Forces and Moments	21
2. Steady Maneuvering Skin Friction.....	24
3. Steady Maneuvering Separation.....	26
4. Maneuvering Pressure Distributions	29
5. Maneuvering Vorticity Flux.....	32
C. Steady Boundary Layer Characteristics.....	33
D. Unsteady Forces and Moments.....	41
1. Unsteady Forces and Moments	41
2. Unsteady Separation.....	45
VI. Conclusions	47

References	48
Appendix A – Ellipsoid Database Generation Script	50
Appendix B – Skin Friction Coefficient Script	52

List of Figures

Figure 1 - Ellipsoidal Model Schematic	5
Figure 2 - Fine Ellipsoid Mesh	6
Figure 3 - Plots of Fine Mesh Surface Curvature and first and second curvature derivatives	7
Figure 4 - Cumulative Distribution Function for the 10° lift coefficient	14
Figure 5 - Skin Friction Coefficients along vertical centerline (RANS-left, LES (Bensow-2009)-right)	15
Figure 6 - Spalart-Allmaras Forward Transition Grid Study	16
Figure 7 - K-O SST Forward Transition Grid Study	17
Figure 8 - Comparison of Skin Friction Calculations – Ludwig and Tillman.....	17
Figure 9 - Skin Friction Grid Convergence Index	18
Figure 10 - Ahead Skin Friction Contour - Upper Surface.....	18
Figure 11 - Skin friction coefficients for exponents of curvature of 2.0 and 2.1	19
Figure 12 - Velocity Profiles along body centerline in the ahead condition.....	20
Figure 13 - Ahead Pressure Distribution (Cp)	21
Figure 14 - Ahead Pressure Gradients	21
Figure 15 - Body fixed coordinate system.....	22
Figure 16 - Normal Force Coefficient vs. Roll Angle	22
Figure 17 - Pitching Moment Coefficient vs. Roll Angle.....	22
Figure 18 -Yaw Moment Coefficient vs. Roll Angle	23
Figure 19 - Side Force Coefficient vs. Roll Angle	23
Figure 20 - Rolling Moment Coefficient vs. Roll Angle	24
Figure 21 - Steady skin friction contour plots of the ellipsoid model upper surface: 15° Yaw Turn	25
Figure 22 - Skin Friction Contour Plots – 10° Yaw.....	25
Figure 23 - Simulated Separation lines vs. Experimental Data - 10° Yaw Case	27
Figure 24 - Simulated Separation lines vs. Experimental Data - 15° Yaw Case	28
Figure 25 - Comparison of turbulence model separation calculations for 15° yaw turn, 25° roll angle	28
Figure 26 - Grid Comparison of separation calculations-15° Yaw and 25° Roll– Spalart-Allmaras Model	28
Figure 27 - Pressure Coefficient Distributions - 15° Yaw Turn	30
Figure 28 - Streamwise and Spanwise Pressure gradients -Upper Surface– 15° Yaw Turn.....	31
Figure 29 - Maximum Spanwise Pressure Gradient vs. Experimental Skin Friction Minima - 15° Yaw Turn	32
Figure 30 - Spanwise Vorticity Flux 15° Yaw Turn.....	32
Figure 31 - Boundary Layer Characteristic Lines: 10° Yaw Turn.....	33
Figure 32 - Steady Momentum Thickness: 10° Yaw Turn, 0-20° Roll	35
Figure 33 - Steady Shape Factor: 10° Yaw Turn, 0-20° Roll	36
Figure 34 - Boundary Layer Characteristic Lines: 15° Yaw Turn.....	37
Figure 35 - Steady Momentum Thickness: 15° Yaw Turn, 0-20° Roll	38
Figure 36 - Steady Shape Factor: 15° Yaw Turn, 0-20° Roll	39
Figure 37 - Steady Edge Velocities 15° Yaw Turn, 5-20° Roll.....	40
Figure 38 - Unsteady Normal Force Coefficients – 10° Yaw Turn	41
Figure 39 - Unsteady Normal Force Coefficients - 15° Yaw Turn.....	42
Figure 40 - Grid study of unsteady normal force coefficients – 15° Yaw Turn	42
Figure 41 - Unsteady Pitching Moment Coefficients – 10° Yaw Turn.....	43
Figure 42 - Unsteady Pitching Moment Coefficients - 15° Yaw Turn	43
Figure 43 - Grid study of unsteady pitching moment coefficients – Spalart-Allmaras model.....	44
Figure 44 - Unsteady Rolling Moment Coefficients – 10° Yaw Turn.....	44
Figure 45 - Unsteady Rolling Moment Coefficients - 15° Yaw Turn.....	45
Figure 46 - Unsteady Separation Positions: 10° Yaw Turn.....	45

List of Tables

Table 1 - Structured Grid Development.....	6
Table 2 - Ahead Drag.....	13
Table 3 - Ellipsoid Model Lift Coefficients.....	14
Table 4 - 10 Degree Lift.....	15

Nomenclature

θ	=	Pitch Angle	FA	=	Frontal Area
ψ	=	Yaw Angle	C_F	=	Force coefficient
ϕ	=	Roll Angle	C_M	=	Moment coefficient
CFL	=	Courant-Friedrichs-Lewy Condition	l	=	Reference length
u	=	Axial velocity	C_f	=	Skin friction coefficient
Δt	=	Time step	τ	=	Shear stress
Δx	=	Grid spacing	U_e	=	Boundary layer edge velocity
E	=	Richardson extrapolation error	U_∞	=	Free-stream velocity
E	=	Relative error	H	=	Shape Factor
p	=	Observed order of accuracy	ν	=	Kinematic Viscosity
r	=	Grid refinement ratio	μ	=	Dynamic Viscosity
GCI	=	Grid Convergence Index	n	=	Exponent of curvature
C_D	=	Drag coefficient	ω	=	Angular velocity
C_L	=	Lift coefficient	f	=	Angular frequency
ρ	=	Fluid density	A	=	Oscillation amplitude

I. Introduction

The study of non Bodies-of-Revolution (non-BOR) has become a prevalent area of interest in naval hydrodynamics. Non-BOR hulls provide equal or greater internal volume with shorter hull lengths than current axi-symmetric designs providing for improved operational capabilities.

Recent efforts into the study of non-BOR submarines have been led by Northrop Grumman Shipbuilding with the Newport-News-Experimental-Models 1 and 2 (NNemo1 and NNemo2). Northrop Grumman efforts have been focused on studying the maneuvering characteristics of the NNemo models utilizing free running lake tests.

The Department of Aerospace and Ocean Engineering at Virginia Tech has also significantly contributed to the understanding of non-BOR hull designs. DeMoss and Simpson studied the wake survey, boundary layer, and skin friction profiles of NNemo1 in the Virginia Tech Stability Wind Tunnel, analyzing the straight and level condition. DeMoss and Simpson¹ also performed a similar study on a non-BOR ellipsoidal model. Granlund and Simpson² and DeMoss and Simpson³ furthered the understanding by performing maneuvering studies on the ellipsoidal model.

Up to this point, the majority of non-BOR studies have been experimental. While experimental studies provide accurate results, the number of cases that can be studied in any given experiment are limited. A key capability of submarine concept design is the ability to examine multiple platform concepts. It is for this reason that this thesis focuses on establishing the ability of Computational Fluid Dynamics (CFD) to simulate the maneuvering characteristics of non-BOR designs. Bensow⁴ performed a preliminary analysis of steady ahead and pitch conditions utilizing the Large Eddy Simulation (LES). This thesis aims to extend his efforts by exploring the feasibility of utilizing the less computationally expensive Reynolds-Averaged Navier Stokes (RANS) models and to provide Reynolds-Averaged boundary layer characteristics and pressure gradient distributions that were not measured experimentally.

II. Literature Review

The only known previous computational modeling of the non-BOR ellipsoid was performed using the Large Eddy Simulation (LES) by Bensow⁴. Bensow utilized a Spalding law-of-the-wall based wall-function with minimum y^+ values of 30 to reduce mesh sizes and limit the computational cost of LES. Calculated lift coefficients showed good agreement with experimental data up to 10 degrees, but deviated thereafter. Persson, Bensow, and Fureby⁵ found there to be evidence that LES and to an extent hybrid RANS/LES could manage three-dimensional flows better than RANS. Bensow's study with wall-functions, however, showed the wall skin friction was significantly under calculated even in the straight and level condition.

Several computational studies have been performed utilizing both RANS and Detached Eddy Simulation (DES) on the 6:1 prolate spheroid. Scott and Duque⁶ performed unsteady modeling of the 6:1 prolate spheroid utilizing both RANS and DES. Their studies showed that Mentor's Shear Stress Transport (SST) model⁷ performed just as well as DES. Both models showed good agreement with pressure distributions, but slightly under calculated the impact of separation on the leeward side. This leads to both models under calculating the total lift on the body and the surface skin friction. Surface skin friction trends though are seen to agree fairly well with experimental results. Pitching moments are also seen to agree well with experimental data. Comparable performance between SST and DES was seen to occur as Scott and Duque commented that even at 20 degrees angle of attack, the 6:1 prolate spheroid did not show regions of massive separation, making it well suitable for RANS.

Rhee and Hino⁸ performed steady and unsteady pitch maneuvering simulations of the 6:1 prolate spheroid utilizing the one equation Spalart-Allmaras turbulence model⁹. Steady simulations showed good agreement with experimental data in normal force and pitching moments up to 10 degrees angle of attack, but under-computed force and moment data for the unsteady maneuvering case. Steady skin friction values also show good agreement with experimental data, but unsteady skin friction tends to not fully capture the unsteady lags. Computational results also generally did not capture the lags in the flow field seen in experimental results due to the delaying of separation in the unsteady case. Rhee and Hino comment that this is due to the isotropic eddy viscosity turbulence model used not adequately resolving the vortical flow on the leeward side of the body. They further state that this is seen to

occur due to the “general tendency of over predicted eddy viscosity in separated regions and the underlying assumption of the turbulence isotropy”.

Simpson¹⁰ also concluded that proper modeling of fully 3-D flows requires turbulence models that not only resolve the near-wall flow, but also account for the anisotropy of Reynolds stresses. Simpson contends that at a minimum, transport equations for $-\overline{uv}$, $-\overline{uw}$, and $-\overline{v^2}$ are required in addition to the momentum and continuity equations. Lowe and Simpson¹¹ continue by contending that accurate modeling of 3D flows is also dependent on the accuracy of the velocity-pressure gradient tensor. This term is shown to highly influence the lag between the mean shear rate and the Reynolds shear stresses, a key modeling problem in 3D flows which is not captured by 1 and 2 equation turbulence models.

The findings of Rhee and Hino and Simpson and Lowe would suggest the usage of an LES model, or at a minimum a hybrid RANS/DES model. An LES model with a fully resolved boundary layer was considered too computationally expensive for concept design and Bensow demonstrated that LES with wall functions significantly under calculates wall skin friction. Scott and Duque demonstrated comparable performance between DES and Mentor’s Shear Stress Transport model suggesting that Mentor’s model might be the best mix of computational cost and accuracy.

III. Simulation Approach

A. Simulation Code

Numerical simulations discussed herein were performed utilizing the NASA developed computational fluid dynamics code, OVERFLOW 2.1.^{12,25} OVERFLOW 2.1 is a Navier-Stokes CFD code for modeling complex geometries utilizing structured, overset (Chimera) grids. The code is capable of modeling 2D, 3D, and Axi-symmetric flows as well as providing modes to support bodies in relative motion. The code provides algebraic, one-equation, and two-equation turbulence models with options for the use of wall functions. A low Mach number preconditioning scheme is available for steady state simulations as well as for dual-time stepping unsteady-time-accurate simulations.

This analysis utilized the Thin-Layer Navier-Stokes Three-Dimensional (TLNS3D) dissipation scheme with the Roe upwind scheme for the Navier-Stokes RHS and the ARC3D diagonalized Beam-Warming scalar pentadiagonal scheme for the conserved q variables where,

$$\frac{\partial q}{\partial t} = - \left[\frac{\partial E}{\partial \xi} + \frac{\partial F}{\partial \eta} + \frac{\partial G}{\partial \zeta} \right] \quad (1)$$

B. Turbulence Models

Two turbulence models were utilized in this analysis. The first turbulence model was Menter's blended 2-equation k- ω SST model⁷, which utilizes k- ω in the near wall region and k- ϵ in the far field. Menter's model was selected as the current literature suggests that it could be a good mix of accuracy and computational cost. The second model used was the one-equation Spalart-Allmaras model⁹, which has shown to produce reliable global force and moment values at a lower computational cost than the two equation SST model. The one equation Spalart-Allmaras model will provide a means of comparison with Mentor's SST model.

C. Model Geometry

The Virginia Tech ellipsoidal model consists of elliptical bow and stern sections with an ellipsoidal cylindrical mid-body, as shown in Figure 1. The bow and stern sections are 0.4 m in length, 0.4 m in width, and 0.231 m in height. Each elliptical section is identical and if connected, would form a 0.8 m long scalene ellipsoid. The parallel mid-body has a cross section

equal to the ends of the bow and stern, which ensures no surface discontinuities occur across the changes in curvature.

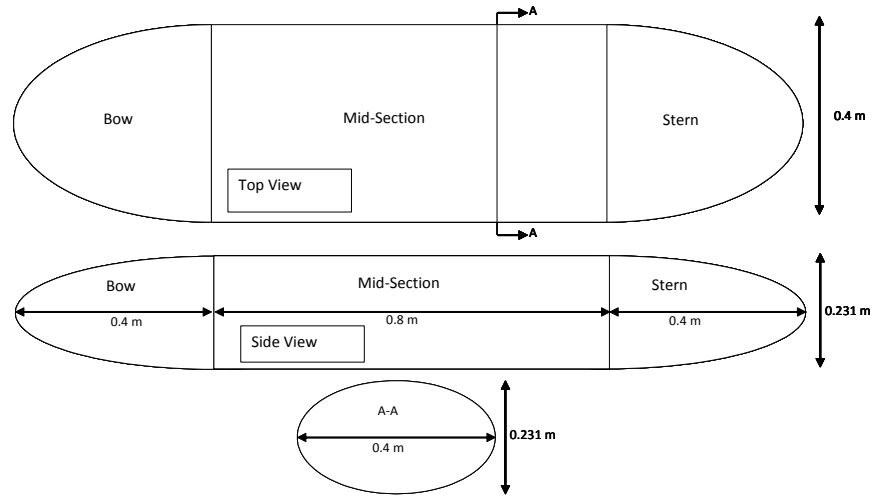


Figure 1 - Ellipsoidal Model Schematic

D. Computational Grids

The use of OVERFLOW 2.1 requires that models be built as structured, overset (Chimera) grids. The grids used in this study were built in accordance with guidance provided by Chan et al.¹³ with four near-body grids and four off-body grids, as shown in Figure 2.

The surface database was constructed utilizing a MATLAB²⁶ script (Appendix A) that had increased refinement around the leading and trailing edges and across the forward and aft changes in body curvature. The database was constructed such that it was four times finer than the finest surface mesh along the forward and aft elliptical ends.

The surface mesh was constructed with four surface grids. The majority of the body was covered by two structured grids spanning from $x/c \sim 0.1$ to $x/c \sim 0.9$ with two additional structured cap grids covering the leading and trailing edges. The two primary grids had 5 cells of interpolation overlap in the spanwise direction with each other and 5 cells of random overlap with the forward and aft cap grids. Spacing across the changes in body curvature was locally refined to 0.002” for the finest mesh with the remaining cells growing away from the refinement utilizing a hyperbolic tangent function. Each near-body grid was extruded normal to the surface to one body diameter to ensure no grid interpolation occurred within the boundary layer.

The first level off-body grid was constructed with cell sizes similar to the outer most cells of the near-body grids. Each additional off-body grid is 2.5 times the size of the previous level,

with the same number of cells, to reduce numerical dissipation and ensure high quality interpolation regions. Off-body blocks were added until the downstream far-field distance reached thirty body lengths. Far-field edges were angled to ensure all sides would act as fully inflow conditions, save the aft most edge.

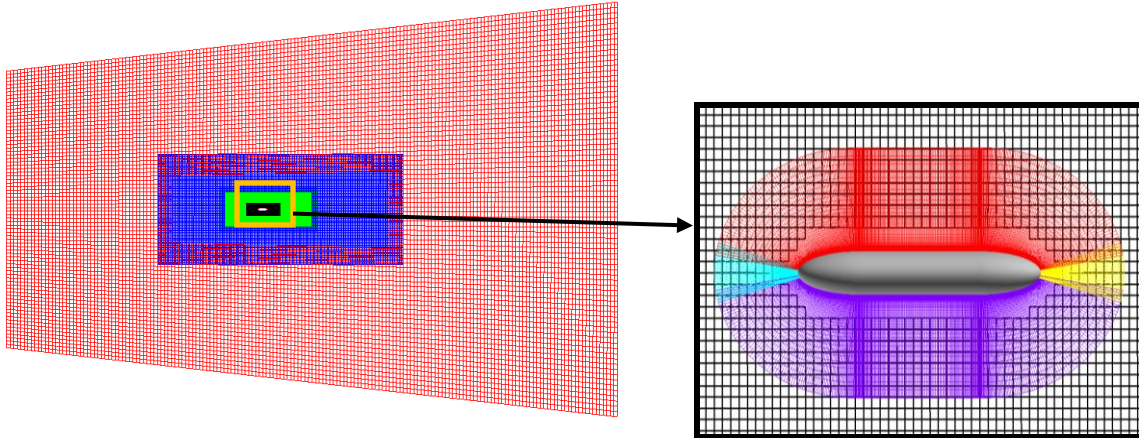


Figure 2 - Fine Ellipsoid Mesh

Three models were generated with a grid refinement ratio of $\sqrt{2}$ for the purpose of estimating the simulation grid uncertainty, as shown in Table 1. The viscous spacing was also refined by the ratio of $\sqrt{2}$, with a maximum initial y^+ value of 1 for the coarse model to accommodate the Spalart-Allmaras model, removing the need for the use of wall functions.

Table 1 - Structured Grid Development

Solution	Name	Initial y^+	Wall			Off Body	Total Nodes
			Normal	Axial	Circumferential		
3	Course	1	40	145	45	93x43x43	1,311,428
2	Medium	0.7071	57	204	64	131x60x60	3,621,024
1	Fine	0.5	80	290	90	185x85x85	9,992,181

Note: Bow and Stern cap grid dimensions not shown

The fine mesh surface was inspected to ensure fairness across the section changes. Figure 3 displays plots of the body curvature as well as the curvature's first and second derivatives. Surface fairness was verified by the curvature's first derivative remaining continuous across the section changes. The body curvature, however, experiences a discontinuity in the second

derivative across the forward and aft section changes. The impact of these discontinuities will be discussed.

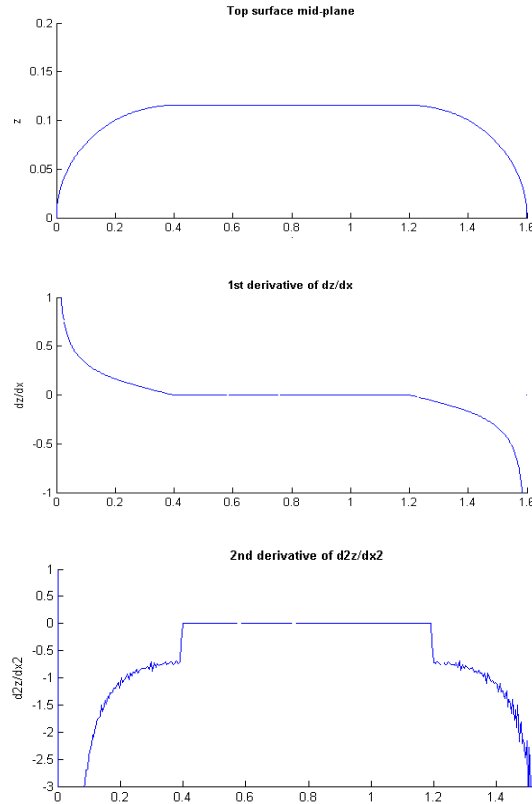


Figure 3 - Plots of Fine Mesh Surface Curvature and first and second curvature derivatives

E. Boundary Conditions

Simulations were run to match the experimental conditions of Demoss and Simpson¹ and Tanious et al¹⁴. Solid wall boundaries were set as viscous adiabatic walls, where pressure was extrapolated. Far-field boundary conditions were set as fully inflow conditions, save the aft most face, which was set as a purely outflow condition, a condition enabled by far-field grid shaping. Inflow angles were established by transforming rotation angles from the vehicle frame into the body frame based on Etkin¹⁵

$$L_{BV} = \begin{bmatrix} \cos\theta\cos\psi & \cos\theta\sin\psi & -\sin\theta \\ \sin\varphi\sin\theta\cos\psi - \cos\varphi\sin\psi & \sin\varphi\sin\theta\sin\psi + \cos\varphi\cos\psi & \sin\varphi\cos\theta \\ \cos\varphi\sin\theta\cos\psi + \sin\varphi\sin\psi & \cos\varphi\sin\theta\sin\psi - \sin\varphi\cos\psi & \cos\varphi\cos\theta \end{bmatrix} \quad (2)$$

where:

θ = Pitch Angle (X1)

ψ = Yaw Angle (X2)

ϕ = Roll Angle (X3)

Steady ahead and pitch simulations were run at a Reynolds number of 4.3 million, corresponding to a free-stream velocity of 44 m/s. Steady and unsteady yaw turn simulations were run at a Reynolds number of 2.5 million and a free-stream velocity of 25.78 m/s. All simulations were run with a kinematic viscosity of $1.65e^{-5}$ m²/s and air density of 1.1 kg/m³.

DeMoss' experimental model included trips at $x/c=0.05$ to ensure turbulent flow over model. The computational model, however, does not include trips. In order to ensure turbulent flow, the free-stream turbulence level was set to 10% and the free-stream turbulent kinetic energy was set to 10^{-6} for the 2-equation SST model. This combination of turbulence settings showed transition to occur around $x/c\sim 0.05$. The turbulence convection terms were solved to the first order for the 1-equation Spalart-Allmaras model and to the second order for the 2-equation SST model.

Unsteady simulations were solved to first order time-accuracy utilizing the Euler implicit scheme. Unsteady time steps were set to achieve a maximum Courant-Friedrichs-Lewy Condition (CFL) of one based on the axial grid length on the ellipsoid fine mesh surface, as recommended by Pandya et al.¹⁶

$$CFL = \frac{u\Delta t}{\Delta x} \quad (3)$$

F. Model Uncertainties

1. Iterative Uncertainty

Iterative uncertainties are neglected in all simulations as residuals converged sufficiently to ignore this uncertainty. Steady ahead simulation residuals were reduced by 13 orders of magnitude. Steady maneuvering simulation residuals were reduced by 8 orders of magnitude. Unsteady maneuvering simulation residuals were reduced by 3-4 orders of magnitude. Additional runs were performed with varying sub-iterations with minimal change in the solution, signifying a satisfactorily converged solution.

2. Grid Uncertainty

A level of numerical uncertainty exists in the simulation due to the necessity of discretizing the model. As the mesh density increases, the level of uncertainty is expected to decrease. An

estimation of grid uncertainties was accomplished through establishing the Grid Convergence Index (GCI) as suggested by Roache.¹⁷ The GCI provides a simple method for reporting grid convergence studies without the restriction of integer level grid refinement. It is based on Richardson extrapolation¹⁷ as it involves the comparison of solutions at different grid refinement levels, but only utilizes the error established by Richardson Extrapolation. The Richardson error estimate is obtained via:

$$E = \frac{|\varepsilon|}{r^p - 1} \quad (4)$$

where:

$$\varepsilon = \frac{f_2 - f_1}{f_1} \quad (5)$$

and:

$$p = \frac{\ln\left(\frac{f_3 - f_2}{f_2 - f_1}\right)}{\ln(r)} \quad (6)$$

where:

f_3 = coarse grid solution

f_2 = medium grid solution

f_1 = fine grid solution

r = grid refinement ratio ($\sqrt{2}$)

The GCI attempts to go beyond the standard error estimation, which provides only 50% error bars, and obtain a confidence level of 95%¹⁷. Roache recommends the use of a safety factor (F_s) of 1.25 to accomplish this end as well as to account for uncertainty in the error estimates, such that

$$GCI = F_s |E| \quad (7)$$

Theoretically, a factor of safety of 1.25 provides 20:1 odds that the solution is bound by the GCI¹⁷, when grid discretization error is considered the primary source of error. The level of confidence is determined by how closely the observed order of accuracy (p) is to the theoretical value. It is shown that the observed order of accuracy is on the order of 2.08, comparing well with the second order solution and providing a high level of confidence that the GCI provides the theoretical 20:1 odds.

IV. Calculation Methods

A. Velocity

OVERFLOW outputs the conserved q variables in matrix form as,

$$q = \begin{bmatrix} \rho \\ \rho u \\ \rho v \\ \rho w \\ \rho e_0 \end{bmatrix} \quad (8)$$

Output velocities are non-dimensionalized based on free stream Mach number, density based on free-stream density, and energy based on the free stream speed of sound. The three non-dimensional velocity components are solved from the conserved q variable matrix as:

$$\begin{aligned} u &= q_2/q_1 \\ v &= q_3/q_1 \\ w &= q_4/q_1 \end{aligned} \quad (9)$$

B. Pressure Coefficient

Utilizing the perfect gas assumption, the non-dimensional static pressure can be solved from the conserved q variables as:

$$\text{Static Pressure} = 0.4(q_5 - \frac{q_1}{2} \left(\left(\frac{q_2}{q_1} \right)^2 + \left(\frac{q_3}{q_1} \right)^2 + \left(\frac{q_4}{q_1} \right)^2 \right)) \quad (10)$$

The pressure coefficient can then be solved as:

$$C_p = \frac{\left(\text{Static Pressure} - \frac{1}{1.4} \right)}{0.5M^2} \quad (11)$$

where:

M = Mach number
Non-dimensional density = 1

C. Wall Shear Stress

Utilizing the non-dimensional velocity components and the local normal vector, the wall shear stress was solved utilizing the FieldView²⁷ script provided in Appendix B. This script is based on the wall shear stress coefficient as outlined by Schetz¹⁸

$$C_f \equiv \frac{\tau_w}{0.5\rho U_e^2} \quad (12)$$

where the wall shear stress is solved as:

$$\tau_w = \mu \frac{\partial U}{\partial y} \quad (13)$$

It should be noted that OVERFLOW assumes a constant non-dimensional viscosity of one.

D. Ludwig-Tillman Shear Stress

Wall shear stress was also established based on the boundary layer profile utilizing the Ludwig-Tillman equation^{19,20}.

$$C_f = 0.246 \times 10^{-0.678H} \left(\frac{U_e \theta}{\delta} \right)^{-0.268} \quad (14)$$

where:

$$\text{Shape Factor (H)} = \delta^* / \theta$$

$$\text{Displacement Thickness } (\delta^*) = \int_0^\delta \left(1 - \frac{u}{U_e} \right) dy$$

$$\text{Momentum Thickness } (\theta) = \int_0^\delta \left(1 - \frac{u}{U_e} \right) \frac{u}{U_e} dy$$

$$\text{Edge Velocity} = U_e$$

Edge velocity was defined as the point in the boundary layer where the u velocity equaled 99% of the local free stream velocity.

It should be noted that the Ludwig-Tillman equation is only valid in the range $U_e \theta / \nu = 10^3$ to 10^4 as noted by Hinze²⁰.

E. Vorticity Flux

Lighthill²¹ showed that the vorticity outwards from a wall can be solved as:

$$-v \left(\frac{\partial w}{\partial z} \right)_0 = -\frac{1}{\rho} (\mathbf{n} \times \nabla) p \quad (15)$$

where:

$$-v \left(\frac{\partial w}{\partial z} \right)_0 = \text{vorticity flux}$$

ρ = density

p = pressure

n = normal vector

F. Maneuvering Characteristics

Maneuvering simulation boundary conditions were rotated to allow for the use of the same model for all cases. Overflow outputs data in the coordinate frame of the model, here always being in the body frame. In order to calculate maneuvering boundary layer characteristics and pressure gradients in line with the free stream frame, output data was transformed into a wall normal coordinate system.

Pressure Gradients

Pressure gradients were first calculated in the body then transformed into the free-stream frame by:

$$\left(\frac{\partial C_p}{\partial x} \right)_{FS} = \left(\frac{\partial C_p}{\partial x} \right)_B \cos(\beta) + \left(\frac{\partial C_p}{\partial z} \right)_B \sin(\beta) \quad (16)$$

$$\left(\frac{\partial C_p}{\partial z} \right)_{FS} = \left(\frac{\partial C_p}{\partial z} \right)_B \cos(\beta) - \left(\frac{\partial C_p}{\partial x} \right)_B \sin(\beta) \quad (17)$$

Boundary Layer Characteristics

Maneuvering velocity profiles were transformed into a wall normal coordinate system to allow for calculating boundary layer characteristics. The transformation matrix provided by equation 2 was used with angles established through the local body derivatives. The local slopes of dy/dx , dy/dz , and dz/dx were established with $\tan^{-1}(dy/dx)$ severing as X3, $\tan^{-1}(dy/dz)$ serving as X1, and $\tan^{-1}(dz/dx)$ severing as X2. This positioned velocity vectors into an ahead wall normal system. Vectors were then translated in the same manner as done for pressure gradients to position them in a free-stream frame.

V. Results and Discussion

A. Steady Ahead

1. Straight Ahead Drag

Straight ahead drag values for all three mesh grids are presented in Table 2. Drag coefficients are non-dimensionalized by the frontal area to provide comparison with the experimental drag. The frontal area drag coefficient was calculated based on:

$$C_{DFA} = \frac{D}{0.5\rho U_{\infty}^2 FA} \quad (18)$$

where the model frontal area was 0.0726 m².

Table 2 - Ahead Drag

Turbulence Model	Coarse	Medium	Fine	GCI	Experiment
		$C_{DFA} = 0.0849$	$C_{DFA} = 0.0849$		$C_{DFA} = \mathbf{0.0852}$
Spalart-Allmaras	$C_{DFA} = 0.0863$	$\epsilon = 0.0165$	$\epsilon = 0$	-	$\mathbf{+/- 0.0136}$
K-omega SST	$C_{DFA} = 0.0856$	$C_{DFA} = 0.0853$ $\epsilon = 0.0035$	$C_{DFA} = 0.0851$ $\epsilon = 0.0024$	0.006	

Both Spalart-Allmaras and K-omega SST show good agreement with the experimental data of DeMoss¹. Spalart-Allmaras shows an error of 0.3%, where K-omega SST shows an error of 0.1%. A grid uncertainty index of 0.006% was calculated for the K-omega SST model, whereas no grid uncertainty could be calculated for Spalart-Allmaras as it demonstrated grid convergence to the significant figures of the experiment.

2. Steady 10 Degree Angle of Attack

Lift and drag values for the ellipsoid's finest model at 10 degrees angle-of-attack are presented in Table 3. Discussions with DeMoss revealed an uncertainty in the free-stream orientation on the order of 1.45 degrees in both yaw and pitch. To account for this uncertainty, a range of pitch and yaw angle conditions were simulated.

Table 3 - Ellipsoid Model Lift Coefficients

Model Orientation		Lift Coefficient		Drag Coefficient	
Pitch Angle	Yaw Angle	Spalart-Allmaras	K-omega SST	Spalart-Allmaras	K-omega SST
10	0	0.295	0.316	0.138	0.146
9	1	0.252	0.274	0.128	0.133
9	0	0.249	0.273	0.127	0.133
8.55	0	0.231	0.253	0.122	0.128
Data – 10 degree AoA		0.270 +/- 0.019		0.112 +/- 0.0136	

The range of conditions bound the experimental lift coefficient with both the Spalart-Allmaras and K-omega SST models as shown in Figure 4. Maximum yaw angles of 1 degree were used as the 1.45 degree range in pitch fully captured the lift coefficient and higher yaw angles would only act to further increase the slightly over predicted drag coefficient. The Spalart-Allmaras model consistently predicted lower lift and drag values than the K-omega SST model. It is difficult to differentiate performance on lift as both models bound the experimental value, but the Spalart-Allmaras model provided a slightly more accurate calculation of the drag coefficient.

CDF - 10 Degree Lift Coefficient

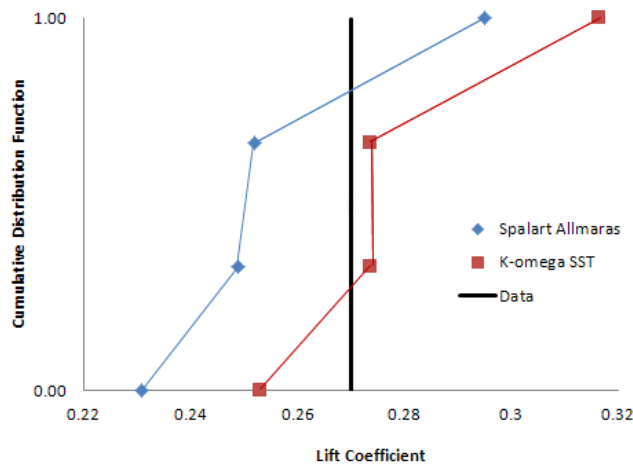


Figure 4 - Cumulative Distribution Function for the 10° lift coefficient

The grid uncertainty in lift coefficient was also established utilizing equations 4-7 in a similar manner to the straight ahead drag. Table 4 shows lift coefficients for the range of grid refinements.

Table 4 - 10 Degree Lift

Turbulence Model	Coarse	Medium	Fine	GCI
		$C_{LFA} = 0.295$	$C_{LFA} = 0.295$	
Spalart-Allmaras	$C_{LFA} = 0.298$	$\epsilon = 0.010$	$\epsilon = 0$	-
K-omega SST	$C_{LFA} = 0.322$	$C_{LFA} = 0.318$ $\epsilon = 0.0126$	$C_{LFA} = 0.317$ $\epsilon = 0.003$	0.0013

The K-Omega SST model again shows low grid uncertainty at the fine mesh level with a GCI of 0.0013%. Also similar to the straight ahead drag condition, the Spalart-Allmaras model demonstrates grid convergence at the fine mesh level.

3. Straight Ahead Skin Friction

Steady skin friction values were studied in the ahead condition and compared to the experimental results of DeMoss¹. Skin friction coefficients along the vertical centerline are plotted in Figure 5 for the K-omega SST model and compared with Bensow’s LES results⁴. Ludwig-Tillmann values are restricted to their valid range.

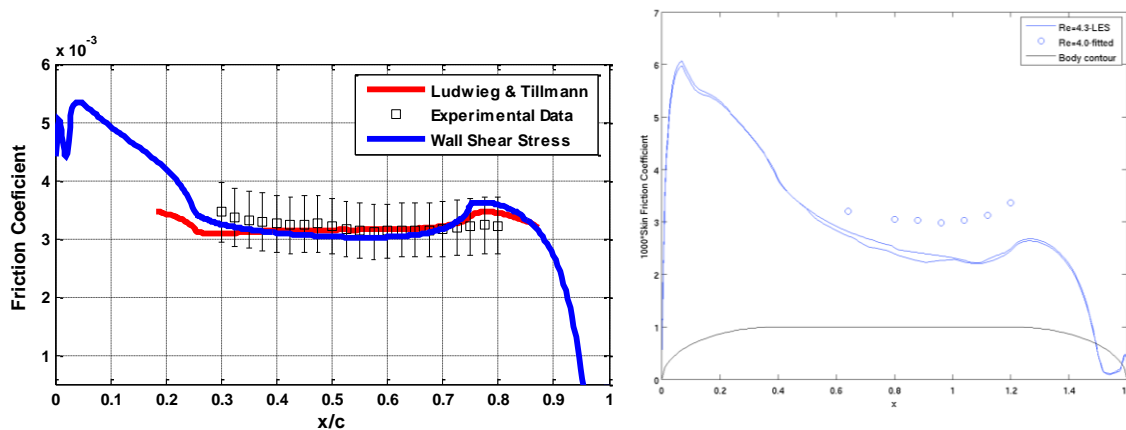


Figure 5 - Skin Friction Coefficients along vertical centerline (RANS-left, LES (Bensow-2009)-right)

RANS skin friction values show excellent agreement with experimental data¹ along the parallel mid-body, showing better agreement than even Bensow's LES solution. It should be noted that Bensow's simulations utilized wall functions with the intent of reducing the computational cost of LES, whereas these simulations fully resolve the boundary layer.

The Ludwig-Tillmann equation slightly under predicts the skin friction across the forward change in curvature and over predicts the aft. The wall shear stress method shows improved agreement across the forward curvature change, but also over predicts across the aft. The jump in shear stress is also experienced in Bensow's results, showing it to not be limited to only RANS.

A 2D grid sensitivity study was performed to ensure this effect was not seen due to a lack of grid refinement across the curvature change. Four grids were generated with grid refinement ratios of $\sqrt{2}$. Both the K- ω SST and Spalart-Allmaras turbulence models were utilized to ensure the condition was not isolated to one model. As shown in Figures 6 and 7, the jump in skin friction across the change in curvature occurs for the full range of mesh densities.

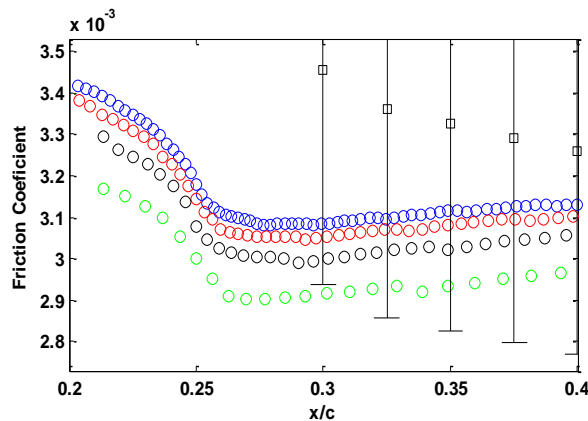


Figure 6 - Spalart-Allmaras Forward Transition Grid Study

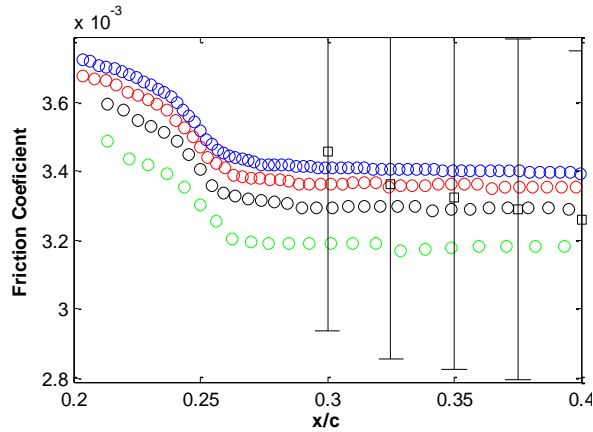


Figure 7 - K-O SST Forward Transition Grid Study

The Spalart-Allmaras model shows slightly less impact across the forward change in curvature than does the K-omega SST model, however, the K-omega SST model shows better agreement with the experiment along most of the parallel mid-body, as shown in Figure 8.

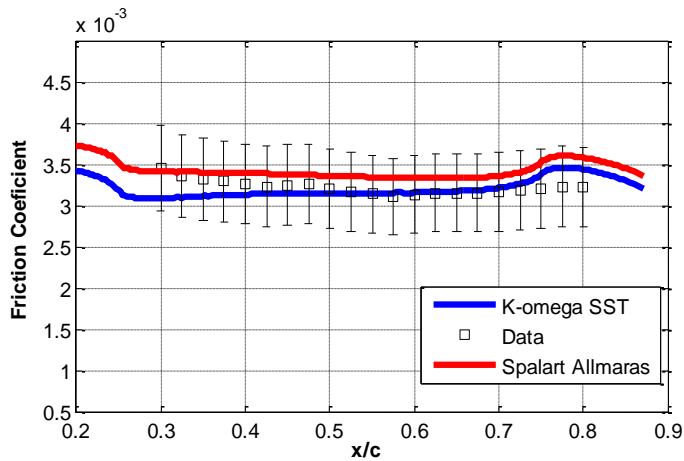


Figure 8 - Comparison of Skin Friction Calculations – Ludwig and Tillman

Roache's Grid Convergence Index¹⁷ was also established for the ahead skin friction. Plotting the GCI with the experimental error bars, Figure 9, shows the simulation to be fully captured by the experimental uncertainty.

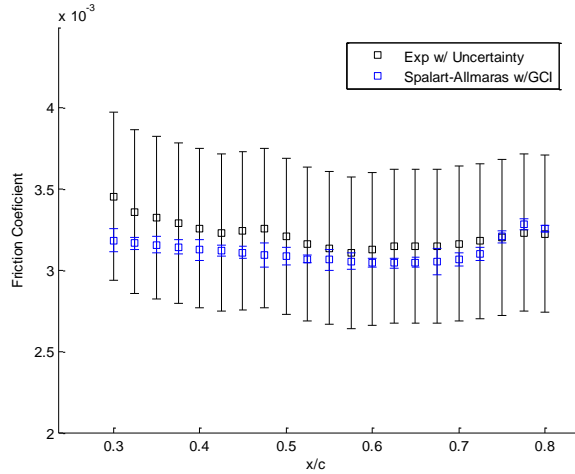


Figure 9 - Skin Friction Grid Convergence Index

The impact across the changes in curvature can also be seen in contour plots of body skin friction as shown in Figure 10.

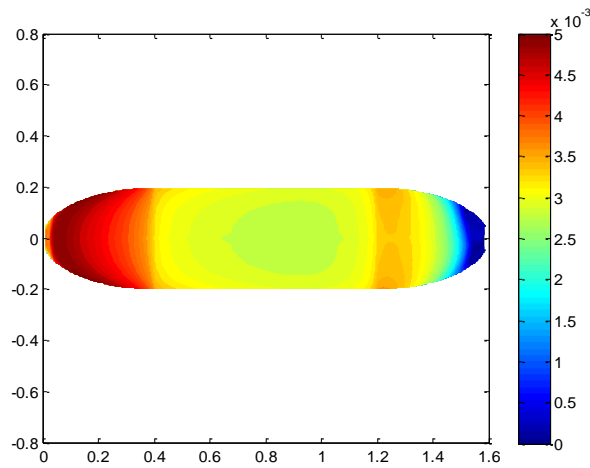


Figure 10 - Ahead Skin Friction Contour - Upper Surface

In order to establish the impact of the discontinuity in surface curvature, the equation for a super-ellipsoid was used to generate a hull similar in shape, but without the discontinuity as shown in equation 19.

$$\left(\frac{X}{L}\right)^n + \left(\frac{Y}{W/2}\right)^n + \left(\frac{Z}{H/2}\right)^n = 1 \quad (19)$$

where:

L = Section length (0.4 m)

W = Section width (0.4 m)

H = Section height (0.231 m)

Discontinuities in $\frac{\partial^2 y}{\partial x^2}$ and $\frac{\partial^2 z}{\partial x^2}$ of equation 19 exist only for n less than or equal to 2.0 (pure ellipsoid). Figure 11 compares skin friction values for exponents of curvature (n) of 2.0 and 2.1. The discontinuity along the vertical centerline was not fully removed due to discretization, but was reduced from 0.7 to 0.2. It is seen that the peak in skin friction was reduced, but that there is still a significant factor that is unexplained.

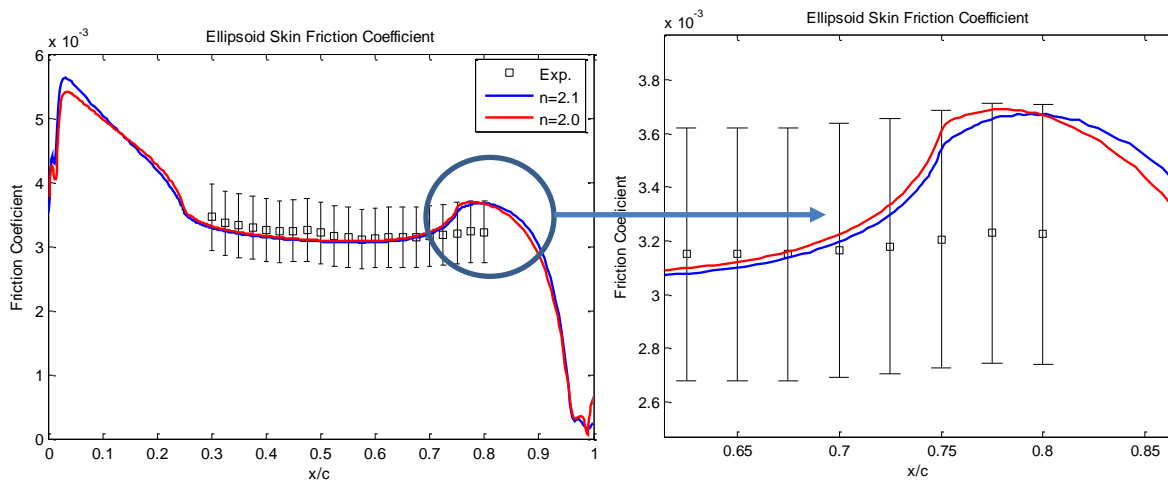


Figure 11 - Skin friction coefficients for exponents of curvature of 2.0 and 2.1

Knight and Zajaczowski²² see a similar localized peak in skin friction in their analysis of a range of stern shapes utilizing the k- ω turbulence model. Knight and Zajaczowski also modeled SUBOFF and showed good agreement with the experimental data, which also included a local peak in skin friction over the aft change in curvature. Knight and Zajaczowski offer no justification for the disagreement between the simulation and experimental data for the range of stern shapes, but do comment that “it is hard to rationalize how a suction peak would not thin the boundary layer and cause a local peak in skin friction.”

It is also seen here that the source for the rise in skin friction is due to a thinning of the boundary layer profile across the change in curvature. Figure 12 shows good agreement with experimental data¹ forward of the change in curvature (x/c = 0.75) with a sudden thinning of the boundary layer directly aft of the change. Thinning of the boundary layer increases the velocity

gradient at the wall and in turn the wall shear stress. No experimental data exists upstream of the parallel mid-body, but a similar yet opposite effect is expected to occur.

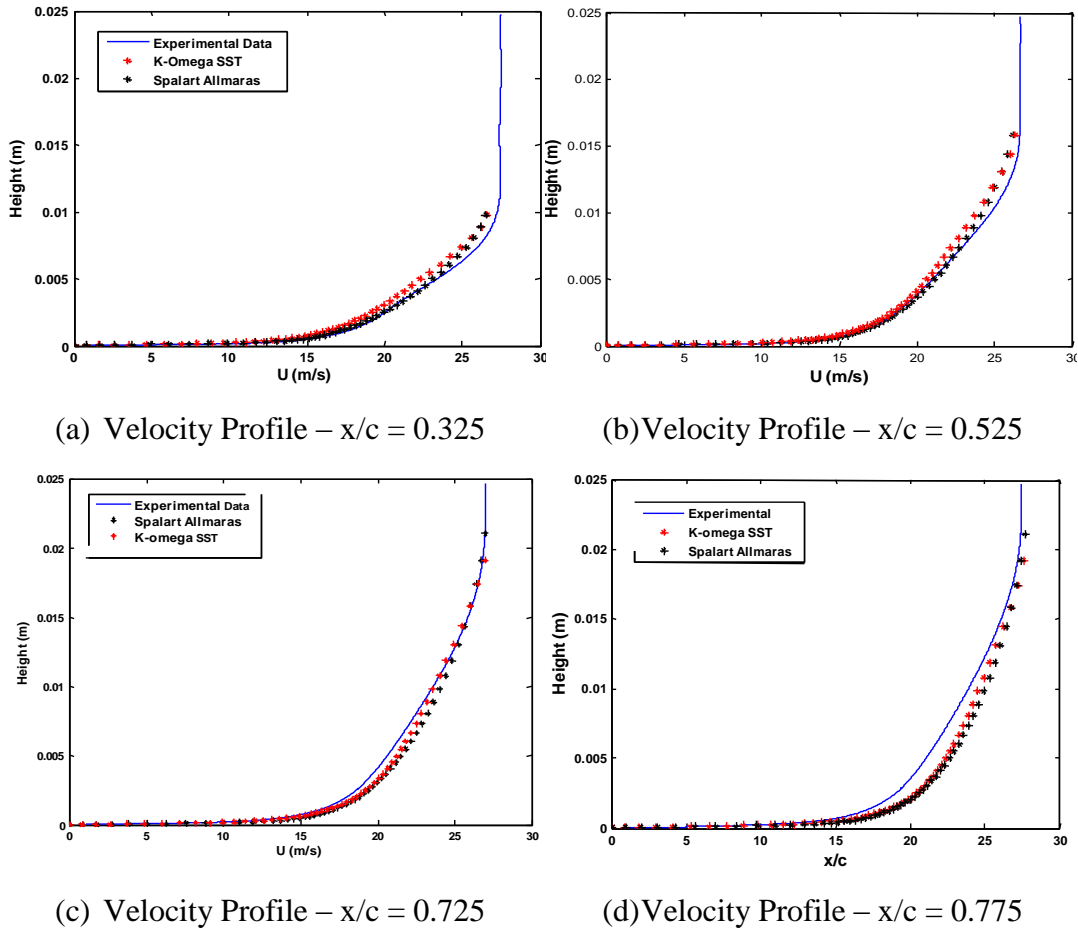


Figure 12 - Velocity Profiles along body centerline in the ahead condition

4. *Straight Ahead Pressure Distributions*

The impact of the change in curvature on the local pressure distribution is seen in Figures 13 and 14. Peaks in the streamwise pressure gradients and local suction pressures occur at both changes in curvature. The impact on the straight ahead pressure distribution is minimal and localized as evidenced by the good agreement with the experimental lift and drag values. The suction peaks are shown, however, to contribute to the local over-calculation of skin friction.

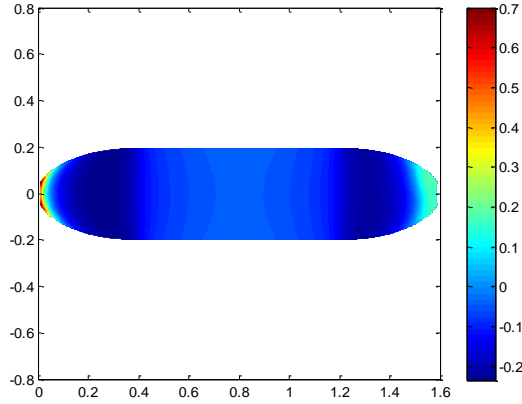


Figure 13 - Ahead Pressure Distrubtion (Cp)

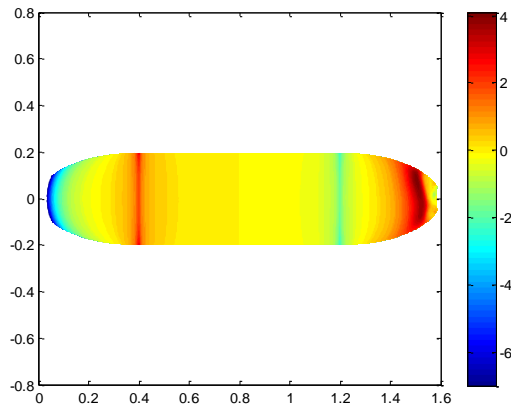


Figure 14 - Ahead Pressure Gradients

B. Steady Maneuvering

1. Steady Maneuvering Forces and Moments

Steady forces and moments for the 10 and 15 degree yaw conditions are presented in Figures 16-20. In these plots, forces and moments are non-dimensionalized based on length (1.6 m), not frontal area.

$$C_F = \frac{Force}{0.5\rho U_\infty^2 l^2} \quad (20)$$

$$C_M = \frac{Moment}{0.5\rho U_\infty^2 l^3} \quad (21)$$

All loads are reported in the body frame with x orientated forward, y oriented out starboard, and z down, as shown in Figure 15. Note that experimental data of Tanious¹⁴ were measured at negative yaw angles. These simulations are performed with positive yaw angles to maintain

consistency with the skin friction results of DeMoss³. Experimental data have been transformed to correspond to positive yaw angles.

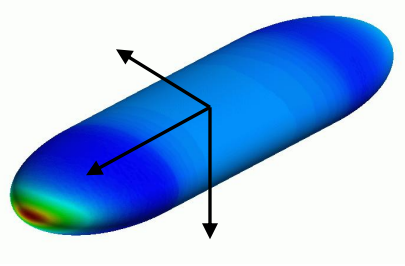


Figure 15 - Body fixed coordinate system

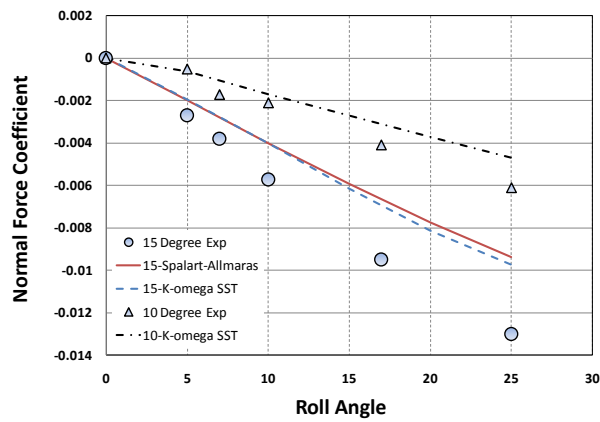


Figure 16 - Normal Force Coefficient vs. Roll Angle

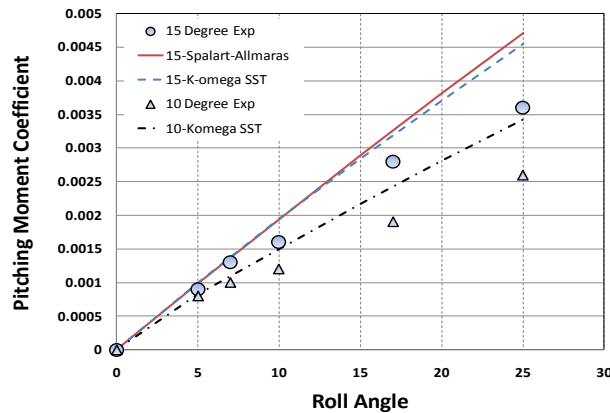


Figure 17 - Pitching Moment Coefficient vs. Roll Angle

Both turbulence models show good agreement for roll angles less than 10 degrees for the normal force coefficient and pitching moment coefficient in the 10 degree yaw case. The normal force and pitching moment coefficients both begin to deviate from the experimental data as roll angles increase beyond 10 degrees. The 10 degree yaw case also shows better agreement than

the 15 degree yaw case. These conditions appear to occur due to the change in curvature's impact on the pressure distribution and the simulated locations of separation. It will be shown later that as rolling and yaw angles increase, the impact of the change in curvature on the pressure distribution increases and the accuracy of the separation location decreases.

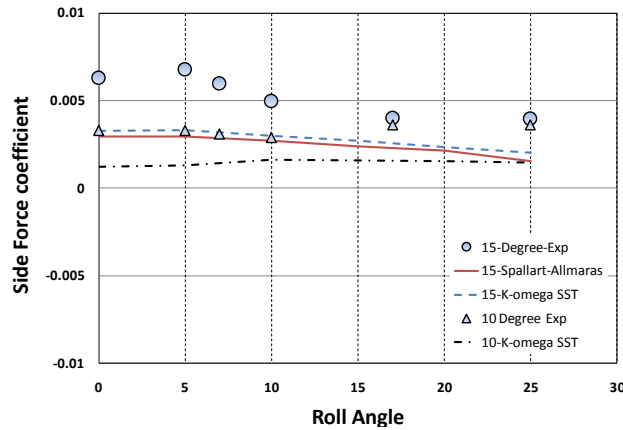


Figure 18 -Yaw Moment Coefficient vs. Roll Angle

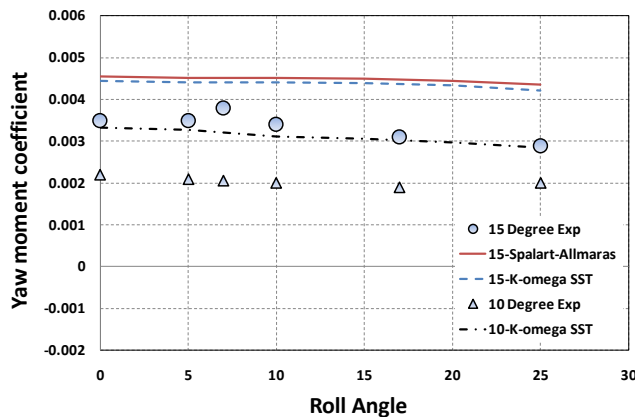


Figure 19 - Side Force Coefficient vs. Roll Angle

Side force and yaw moment coefficients both show general trend agreement with the experimental data, but under and over predict, respectfully, the experiment. These values are strongly affected by cross flow separation and the recirculation regions on the leeward side of the model. Discussions with Buning, developer of OVERFLOW, revealed that modeling separated flow regimes with RANS can be a significant challenge. Mesh densities sufficient to accurately capture separation regions could prove computationally prohibitive. The ability to accurately predict cross flow separation will also be further discussed.

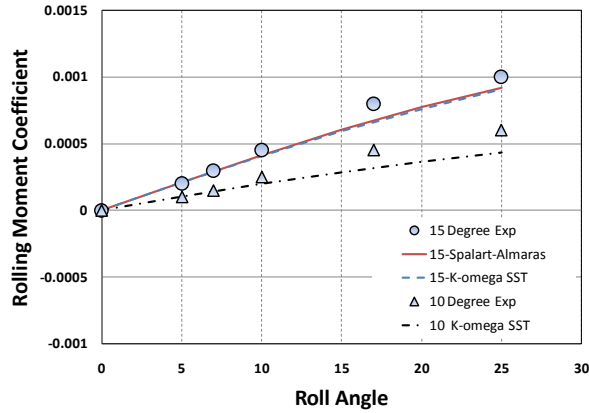
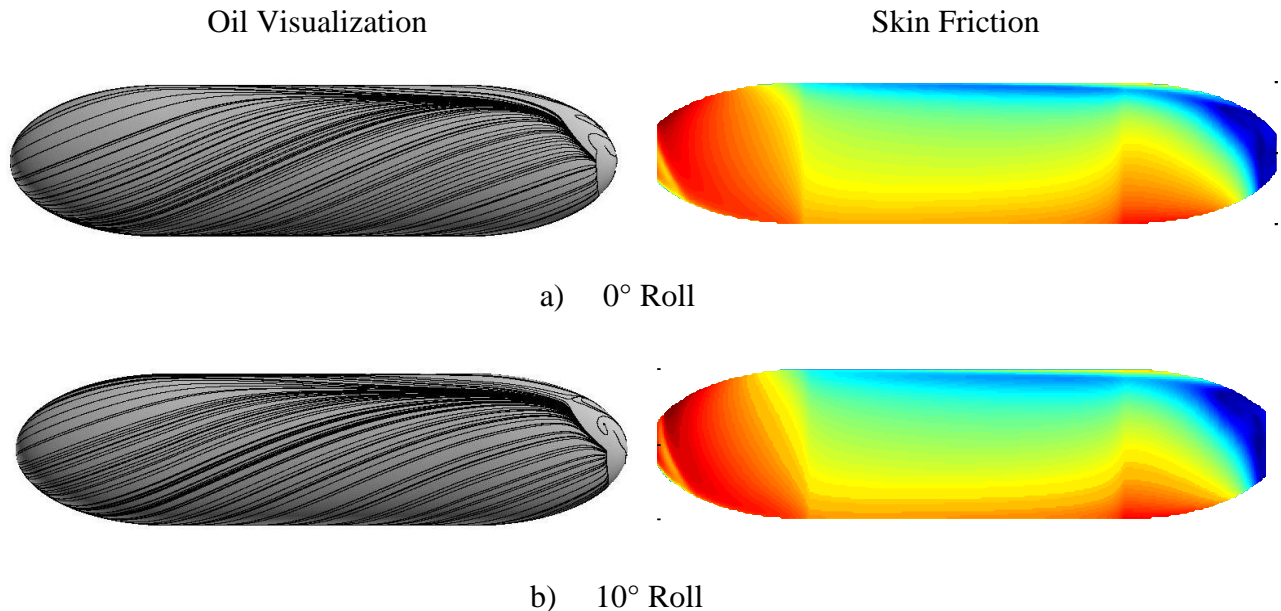


Figure 20 - Rolling Moment Coefficient vs. Roll Angle

The rolling moment coefficient shows good agreement with experimental data for roll angles less than 10 degrees for both the 10 and 15 degree yaw cases. It should be noted that most submarine designs desire to limit turning roll angles to less than 10 degrees for maximum effort turns, a range for which the simulations produce good agreement with experimental data.

2. Steady Maneuvering Skin Friction

The skin friction values for the 10 and 15 degree yaw turns were studied to establish regions of separation and aid in studying the yaw turn forces and moments. Figure 21 shows skin friction coefficients and oil visualizations for the 15 degree yaw turn. All skin friction values presented utilize the wall shear stress method.



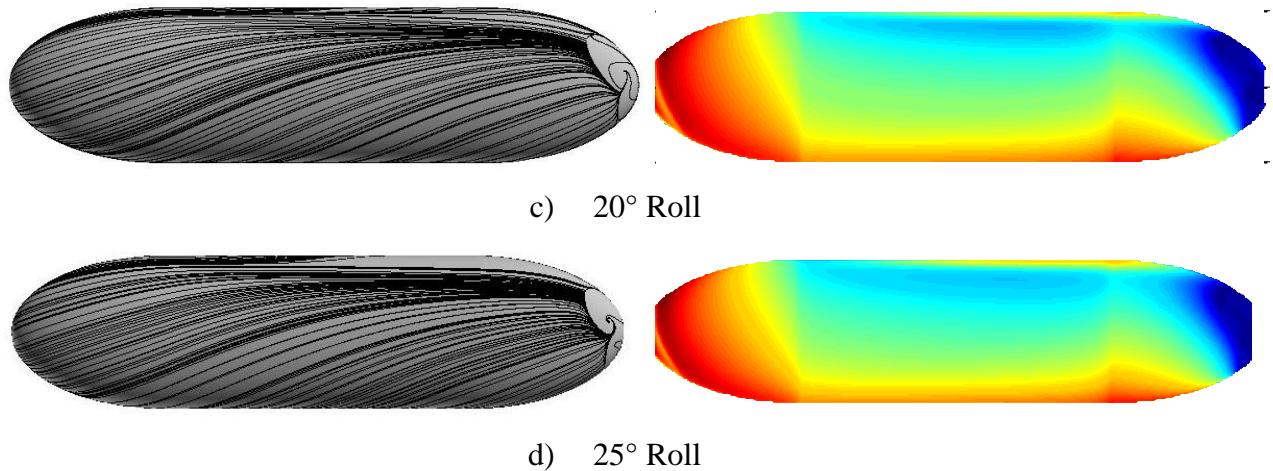


Figure 21 - Steady skin friction contour plots of the ellipsoid model upper surface: 15° Yaw Turn

The impact of the changes in curvature is more pronounced in the yaw condition than the ahead. The localized peak in skin friction influences the inboard skin friction values and forces the skin friction minima further outboard. This impacts the simulated separation line as according to Wetzel²³, the cross flow separation line can be approximated by the circumferential minima in skin friction. Oil visualizations also confirm the locations of minimum skin friction to be separation locations as seen by the converging oil streaks.

Contours of steady skin friction for the 10 degree yaw case are plotted in Figure 22.

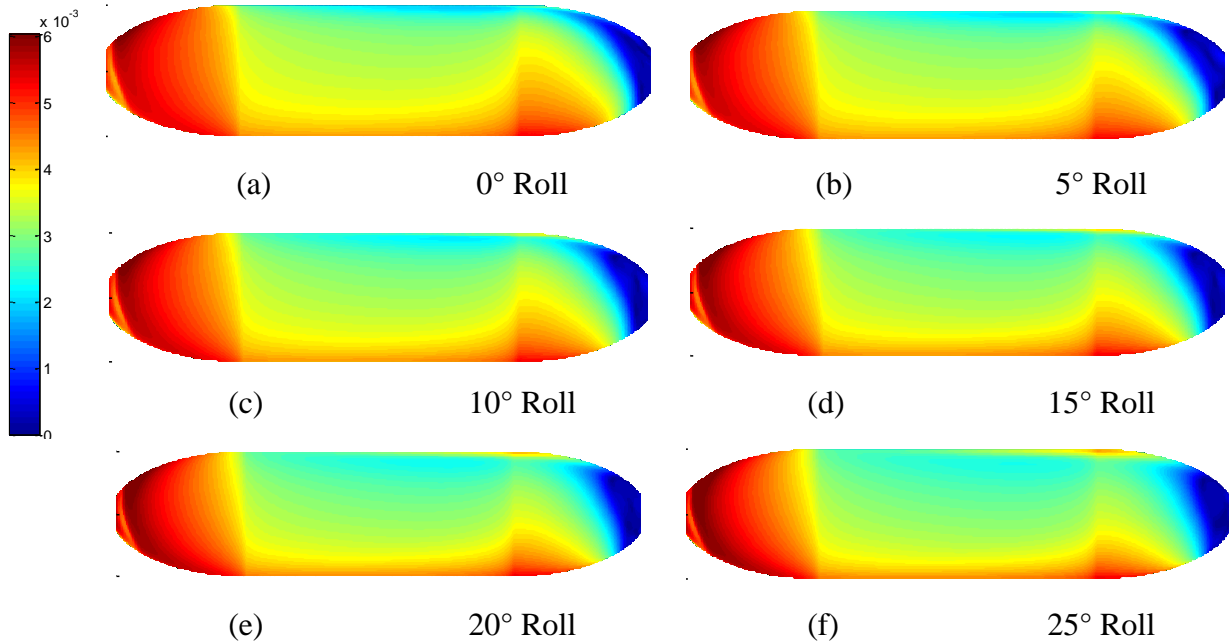
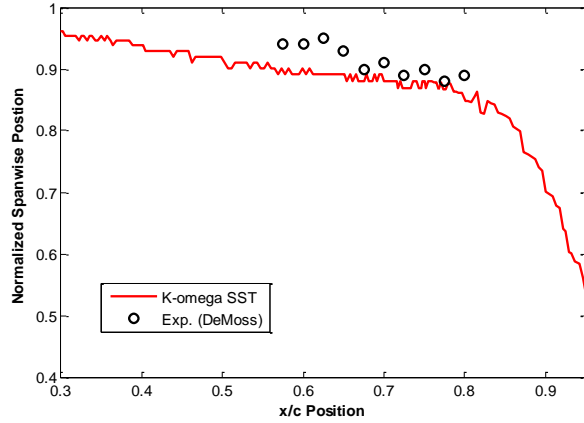


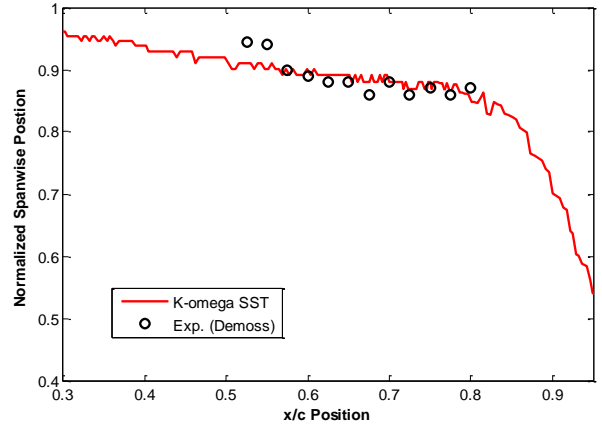
Figure 22 - Skin Friction Contour Plots – 10° Yaw

3. Steady Maneuvering Separation

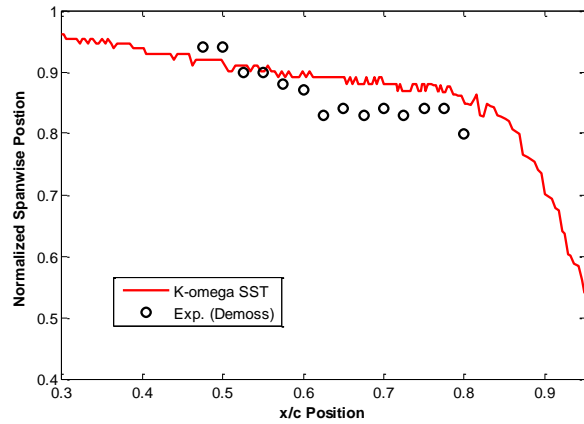
Simulated separation lines for the 10 degree yaw turn show good agreement with the experiment³ for the 5 and 10 degree roll case with errors on the order of 5%. Good agreement is also seen for the 15- 25 degree roll cases up to $x/c \sim 0.5$. Aft of this position, separation lines begin to deviate due to the impact of the aft skin friction peak. Separation moves inboard as the roll angle increases, but the deviation also increases as roll angle increases beyond 10 degrees.



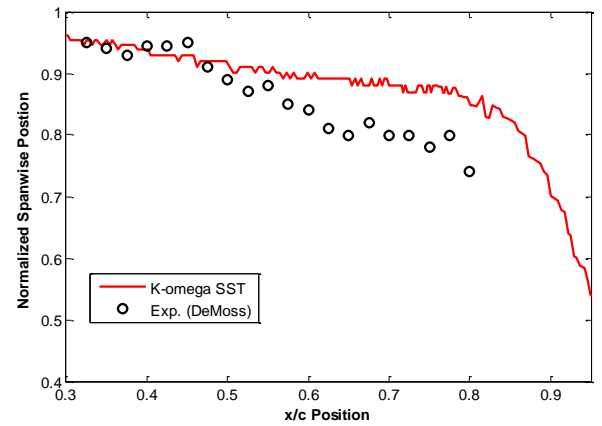
(a) 5° Roll Angle



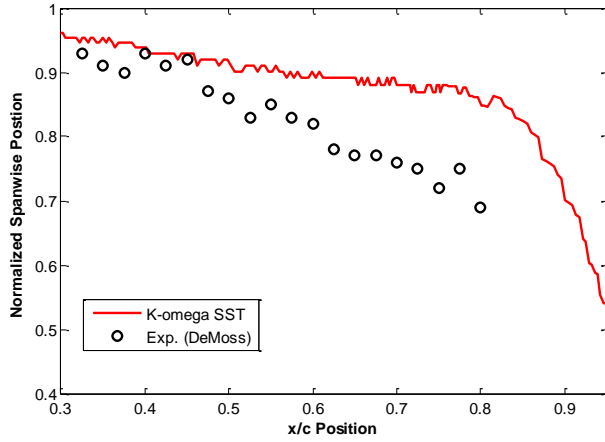
(b) 10° Roll Angle



(c) 15° Roll Angle



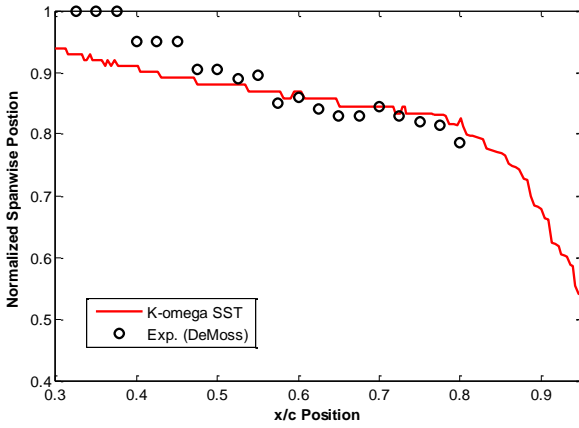
(d) 20° Roll Angle



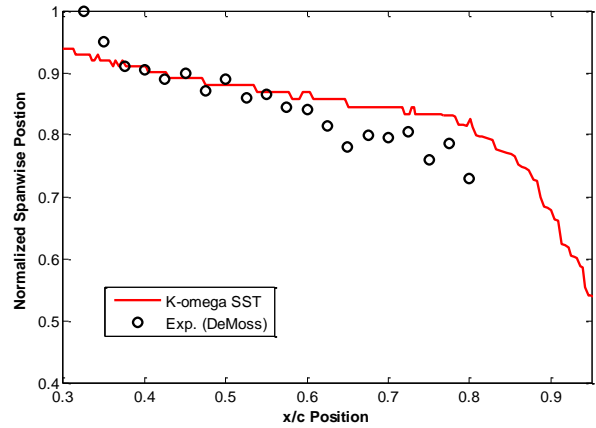
(e) 25° Roll Angle

Figure 23 - Simulated Separation lines vs. Experimental Data - 10° Yaw Case

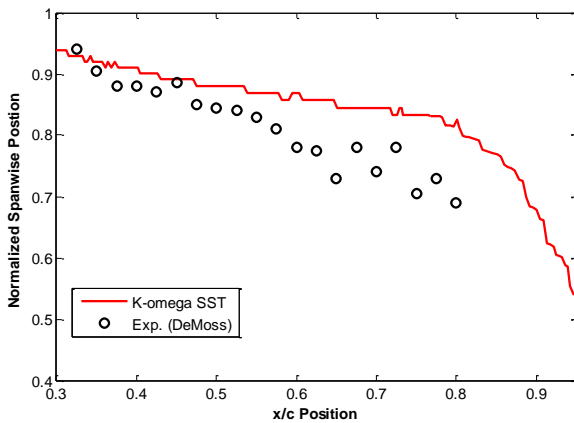
The simulated locations of separation for the 15 degree yaw case also shows good agreement with the experimental separation for roll angles less than 10 degrees.



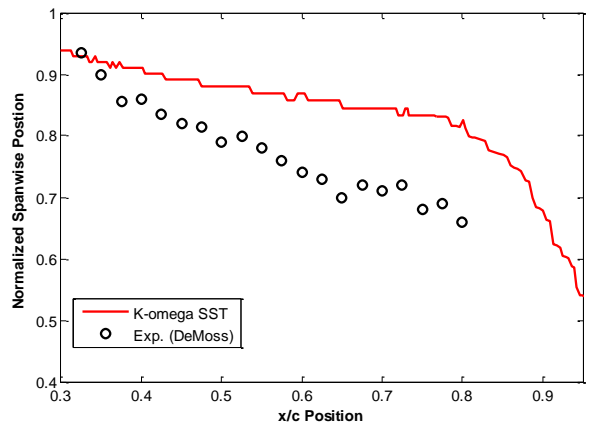
(a) 5° Roll Angle



(b) 10° Roll Angle



(c) 15° Roll Angle



(d) 20° Roll Angle

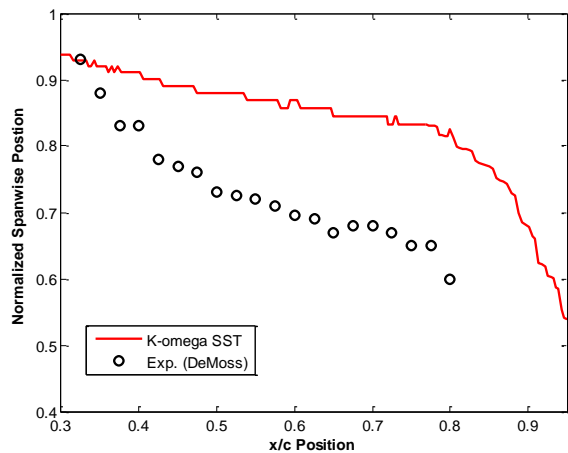


Figure 24 - Simulated Separation lines vs. Experimental Data - 15° Yaw Case

(e) 25° Roll Angle

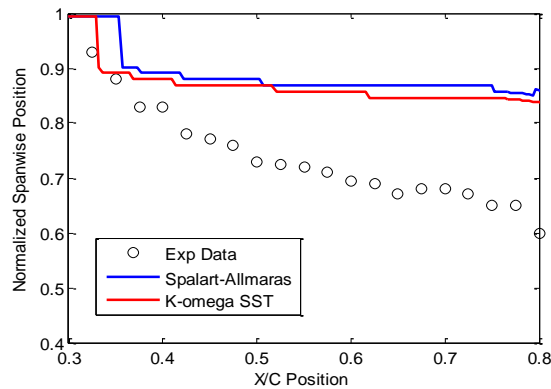


Figure 25 - Comparison of turbulence model separation calculations for 15° yaw turn, 25° roll angle

K-omega SST and Spalart-Allmaras models show similar performance while computing separation locations, as shown in Figure 25. The K-omega SST model locates the forward most separation point more accurately than Spalart-Allmaras, but shows similar performance in computing spanwise separation positions for the 15 degree yaw case.

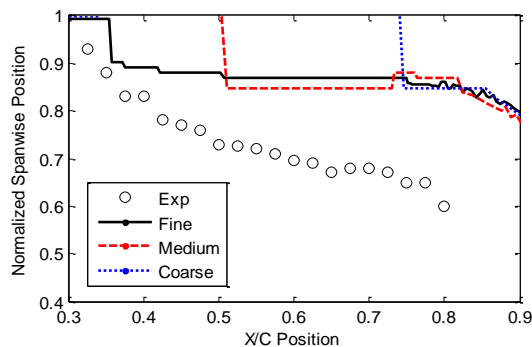


Figure 26 - Grid Comparison of separation calculations-15° Yaw and 25° Roll- Spalart-Allmaras Model

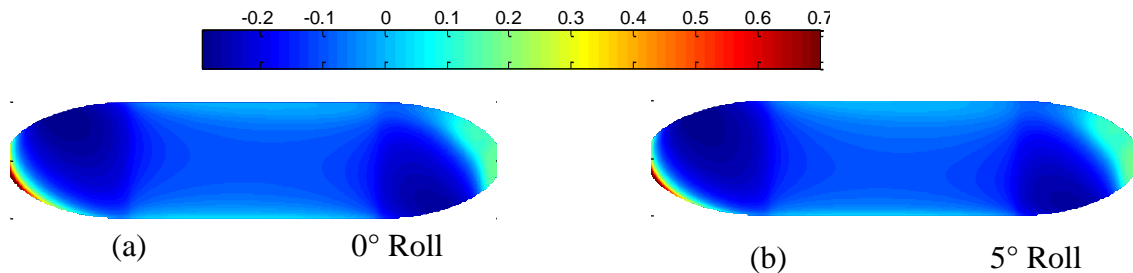
Figure 26 presents separation calculations for the three grid refinement levels utilizing the Spalart-Allmaras turbulence model. It is clear that grid refinement aids in the computation of the initial separation point. The fine mesh shows good agreement with the experiment in locating the forward most location of separation. The error in calculation of the forward most separation point increases as the mesh refinement decreases, however the spanwise locations tend to change very little.

The simulation of separation locations for higher yaw and roll angles reveal the limitations of the 1 and 2 equation turbulence models. Simulations of yaw and roll angles of 10 degrees and less show good agreement with experimental data, which leads to good force and moment data agreement. Simulation performance for maneuvering angles greater than 10 degrees, however, decreases as the three-dimensionality of the flow increases and the impact of the change in curvature becomes more pronounced.

4. *Maneuvering Pressure Distributions*

Pressure Coefficients

Body pressure coefficients for the 15 degree yaw case are shown in Figure 27. Increases in body suction pressure are noticeable across the changes in curvature and become increasingly pronounced as roll angle increases. These artificial suction pressures, especially across the aft end, contribute to the error in the forces and moments increasing as roll angle increases. Increased suction contributes to the under-calculation of the normal force values. Increased suction over the aft end contributes to the under-calculation of the pitch moment. Increased suction loads on the leeward side of the model contribute to the over-calculation of the side force and the increase over the leeward side's aft end contributes to the under-calculation of the yaw moment. It is also seen that due to the curvature change, the suction peak is spread across the span, contributing to the under-calculation of the rolling moment.



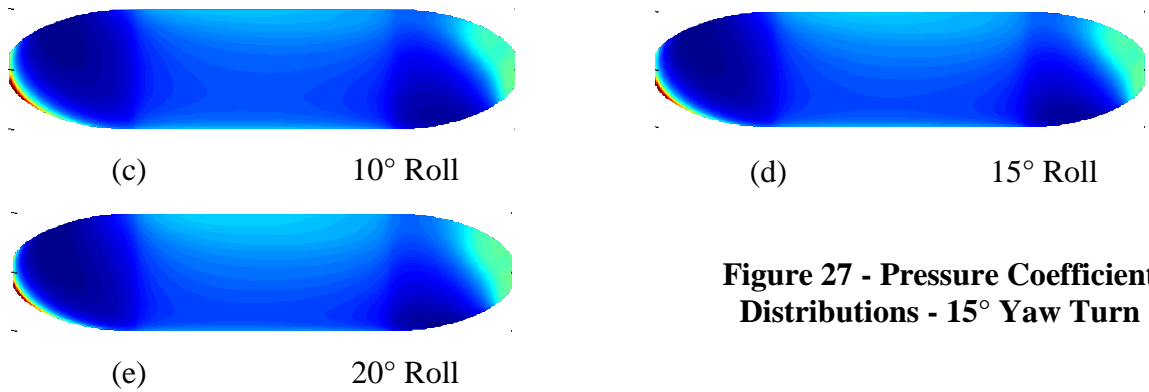


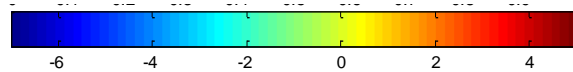
Figure 27 - Pressure Coefficient Distributions - 15° Yaw Turn

Pressure Gradients

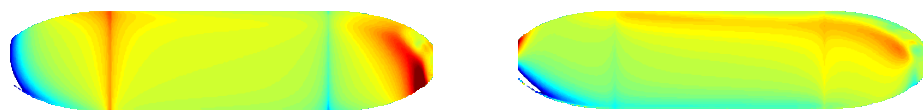
Oil visualizations, as shown in Figure 21, show significant levels of cross flow on the leeward side of the model. Exploring the streamwise and spanwise pressure gradients gives insight into the source of the flow three-dimensionality.

Contour plots of the non-dimensional pressure gradients show regions of adverse streamwise pressure gradient moving inboard as roll angles increase. The peak regions of spanwise pressure gradient are also seen to move inboard as roll angles increase.

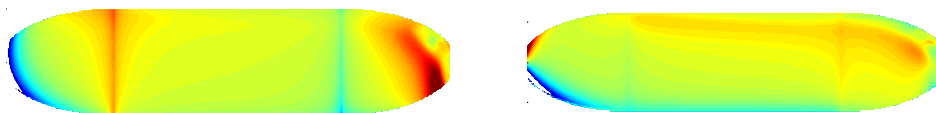
Streamwise Pressure Gradient Spanwise Pressure Gradient



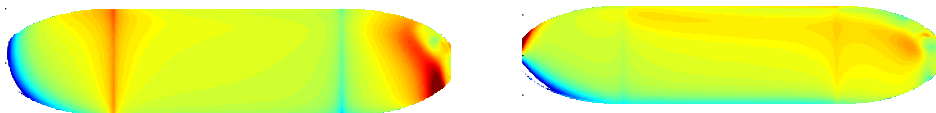
(Non-Dimensional)



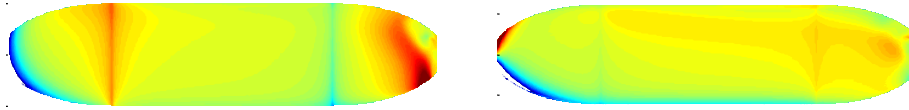
(a) 15° Yaw Turn, 0° Roll



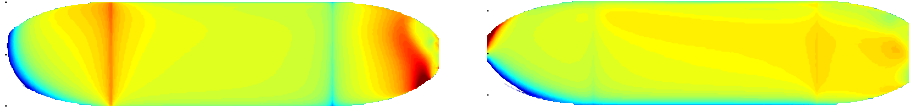
(b) 15° Yaw Turn, 5° Roll



(c) 15° Yaw Turn, 10° Roll



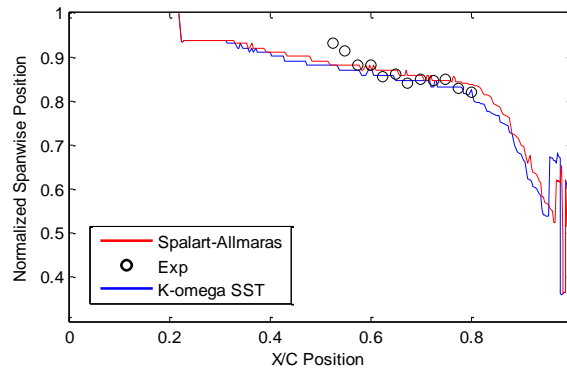
(d) 15° Yaw Turn, 15° Roll



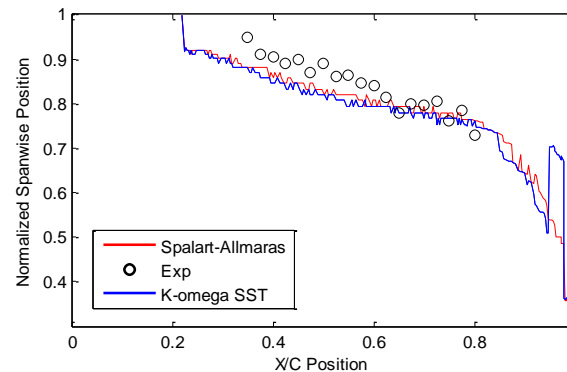
(e) 15° Yaw Turn, 20° Roll

Figure 28 - Streamwise and Spanwise Pressure gradients -Upper Surface– 15° Yaw Turn

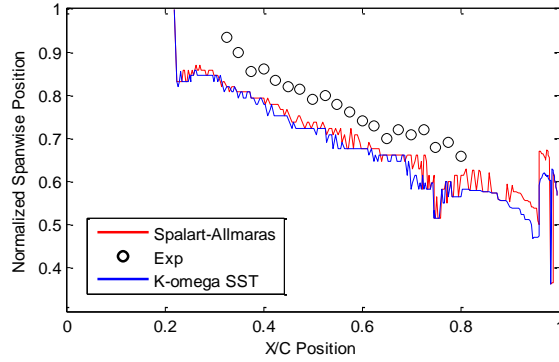
The combination of adverse streamwise pressure gradients and large spanwise pressure gradients causes the boundary layer to skew in 3D and eventually separate. Comparison of the locations of maximum spanwise pressure gradient and experimental locations of separation shows good agreement. This trend agrees with Simpson’s¹⁰ findings where, “Surface pressure fluctuations often reach local maxima in the vicinity of separation and reattachments”, but are not uniquely related to pressure gradients.



(a) 0° Roll Angle



(b) 10° Roll Angle



(c) 20° Roll Angle

Figure 29 - Maximum Spanwise Pressure Gradient vs. Experimental Skin Friction Minima - 15° Yaw Turn

This should not suggest that large spanwise pressure gradients in the presence of adverse streamwise gradients be used as criteria for predicting cross flow separation though, as Simpson goes on to comment that surface pressure fluctuations “are not as sensitive as shear stress measurements” to separation regions.

5. *Maneuvering Vorticity Flux*

Spanwise pressure gradients in the presence of adverse streamwise pressure gradients have been shown to significantly skew the boundary layer. This skewing of the boundary layer leads to increases in the local spanwise vorticity, or a vorticity flux as shown in Figure 30. Increased vorticity leads to the flow spinning up and forming a vortex, the mechanism through which the spanwise pressure gradient is able to influence the separation location.

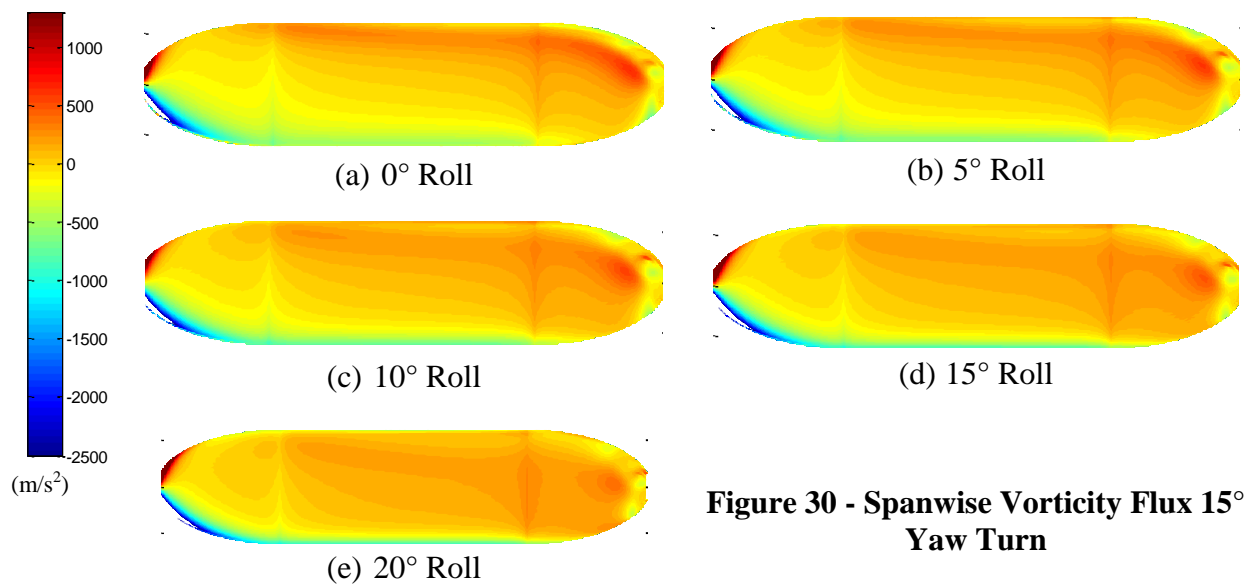


Figure 30 - Spanwise Vorticity Flux 15° Yaw Turn

C. Steady Boundary Layer Characteristics

Boundary layer characteristics for the 10 and 15 degree yaw turn cases were established to provide data that was not collected experimentally. It is desired to relate the integral boundary layer behavior between steady and unsteady cases in order to establish a means of relating the boundary layer behavior to the separation location. While two-dimensional boundary layer separation criteria are not fully applicable due to the three-dimensionality of the flow, it is desired to develop a heuristic or phenomenological understanding between the boundary layer behavior and separation once the unsteady experimental data is fully processed.

Seven parallel lines, in line with the free-stream flow, were chosen to establish boundary layer trends, as shown in Figure 31. Each line is equally spaced 0.025 m apart with the first line starting at the forward perpendicular.

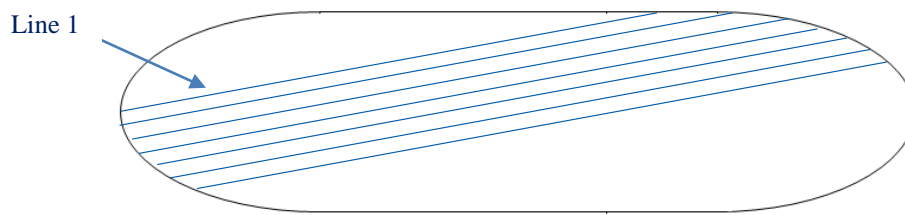
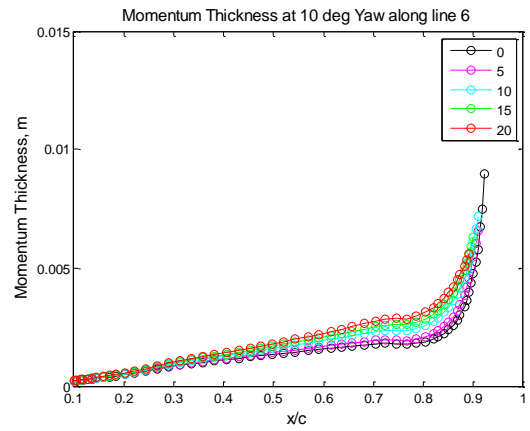
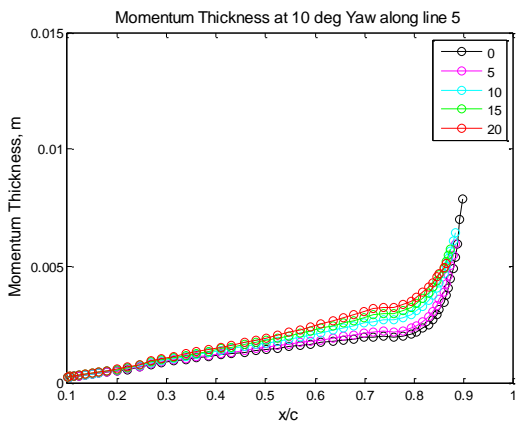
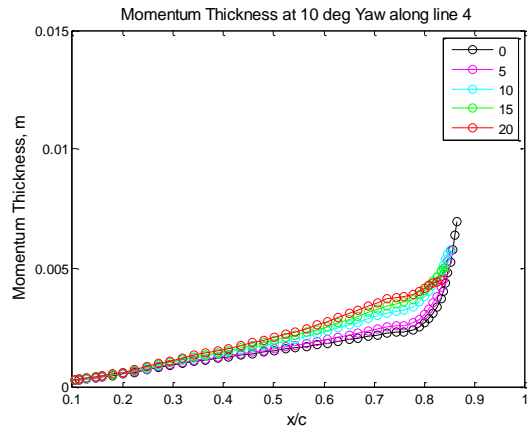
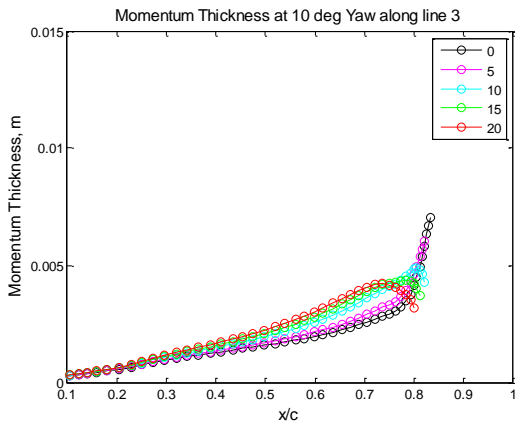
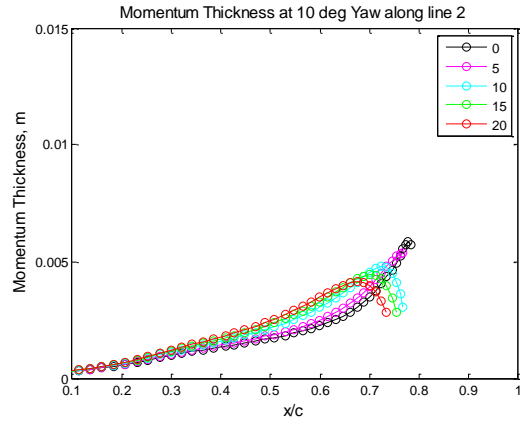
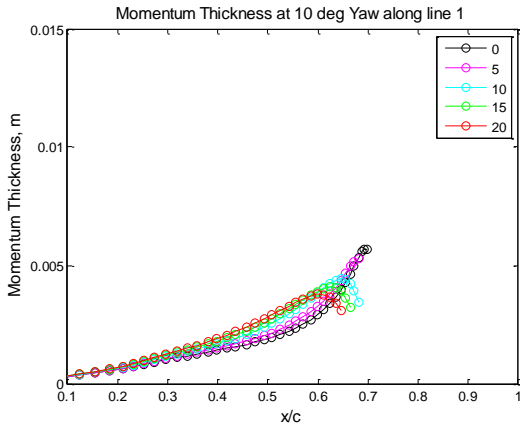


Figure 31 - Boundary Layer Characteristic Lines: 10° Yaw Turn

Momentum thickness for the 10° yaw case is presented in Figure 32 for roll angles 0-20°. It is seen that momentum thickness increases with increasing roll angle. The forward change in curvature doesn't appear to significantly impact the momentum thickness; however the aft curvature change has a clear impact. Lines 4-7 show a distinct bend in the curves across the aft change in curvature. This is seen to occur due to the thinning of the boundary layer across the curvature change, which locally decreases the momentum thickness.



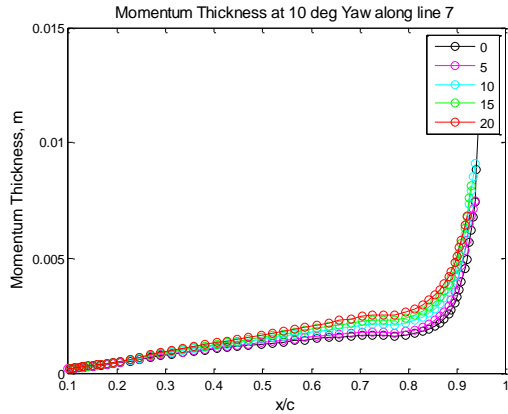
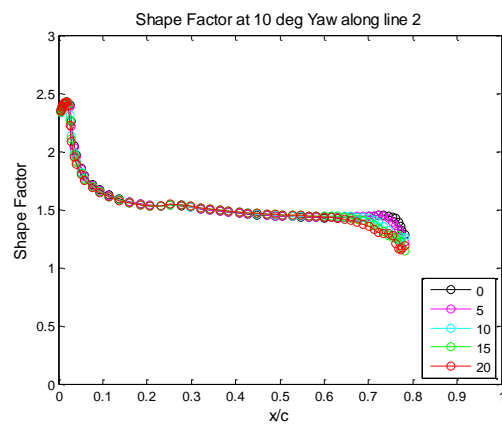
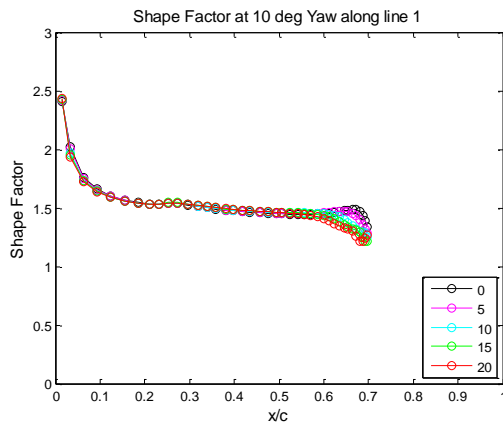


Figure 32 - Steady Momentum Thickness: 10° Yaw Turn, 0-20° Roll

Boundary layer Shape Factors are plotted in Figure 33 for the 10° yaw case. Laminar flow is seen to exist on the most forward section of the model with shape factors on the order of 2.5-2.6²⁴. Flow quickly trips to turbulent around $x/c=0.05$, as seen by the abrupt drop in shape factor to values in the range of 1.5²⁴. The local high streamwise pressure gradient experienced across the forward change in curvature is seen through the minor local increase in shape factor. Von Karman’s momentum integral equation for two-dimensional incompressible flows²⁴ can be solved to show that the shape factor can be increased by increasing the streamwise pressure gradient.

$$\text{Von Karman momentum integral equation: } \frac{d\theta}{dx} = \frac{\theta}{q} \frac{dp}{dx} \left(1 + \frac{H}{2}\right) + \frac{\tau_w}{2q} \quad (21)$$

Conversely, the decreasing pressure gradient aft of the forward change in curvature decreases the shape factor. It should be remembered that the shape factor is truly a two-dimensional flow parameter and its validity decreases as the three-dimensionality of the flow increases.



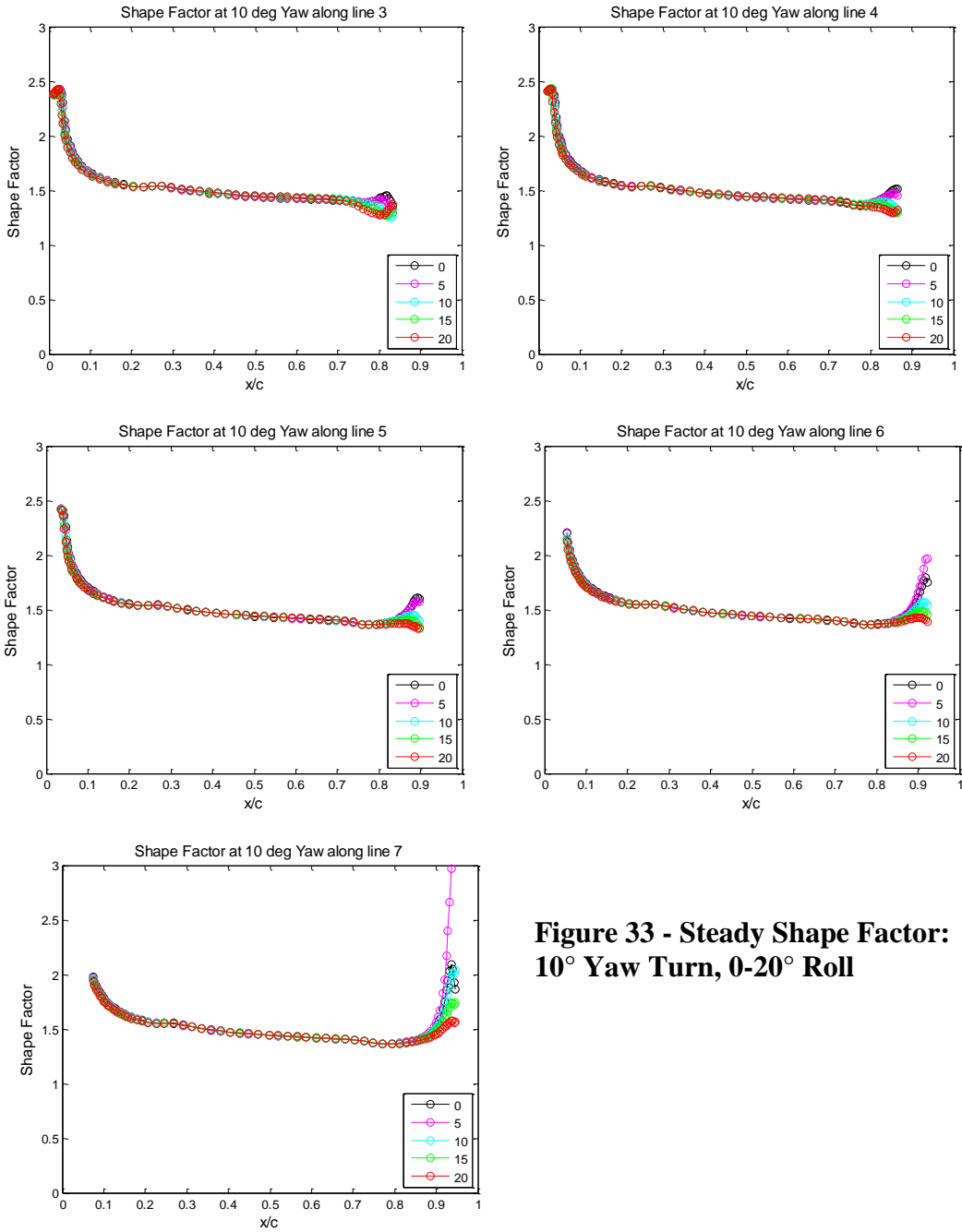


**Figure 33 - Steady Shape Factor:
10° Yaw Turn, 0-20° Roll**

Boundary layer characteristics for the 15° yaw turn case are presented below. These plots reveal additional boundary layer trends across the midbody. The data's validity is more limited than the 10° case, however, due to the flow becoming three-dimensional further inboard.

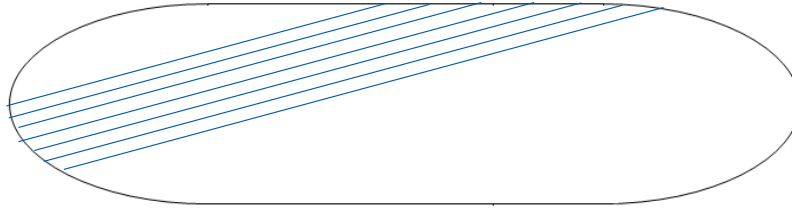
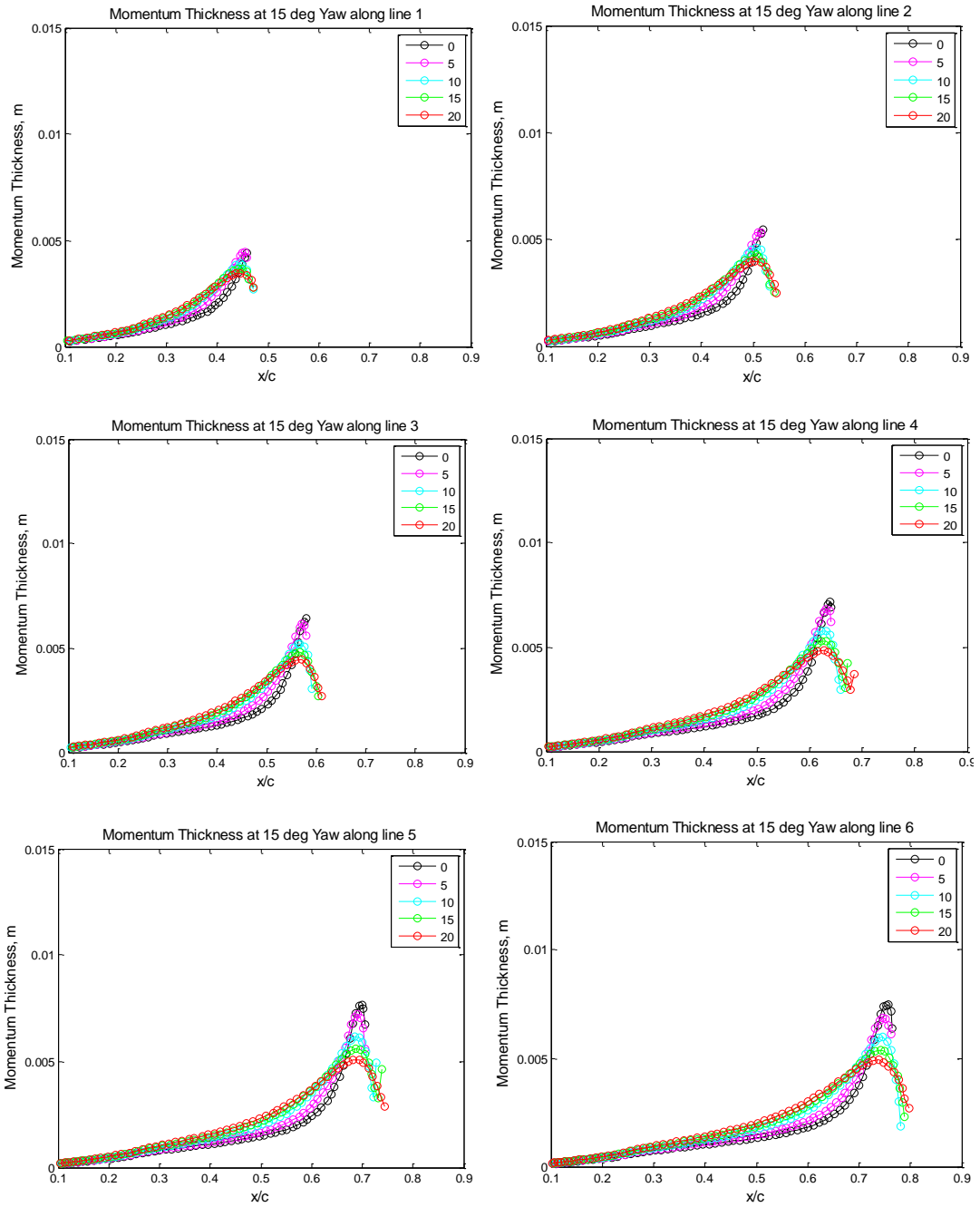


Figure 34 - Boundary Layer Characteristic Lines: 15° Yaw Turn



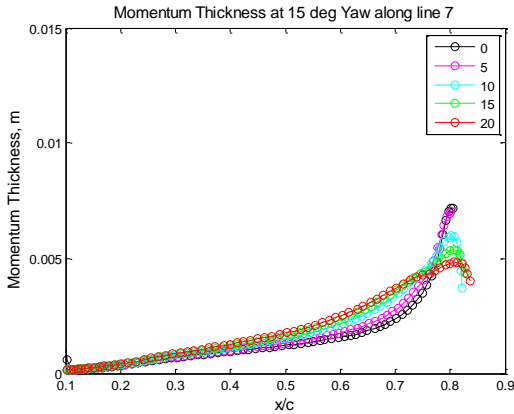
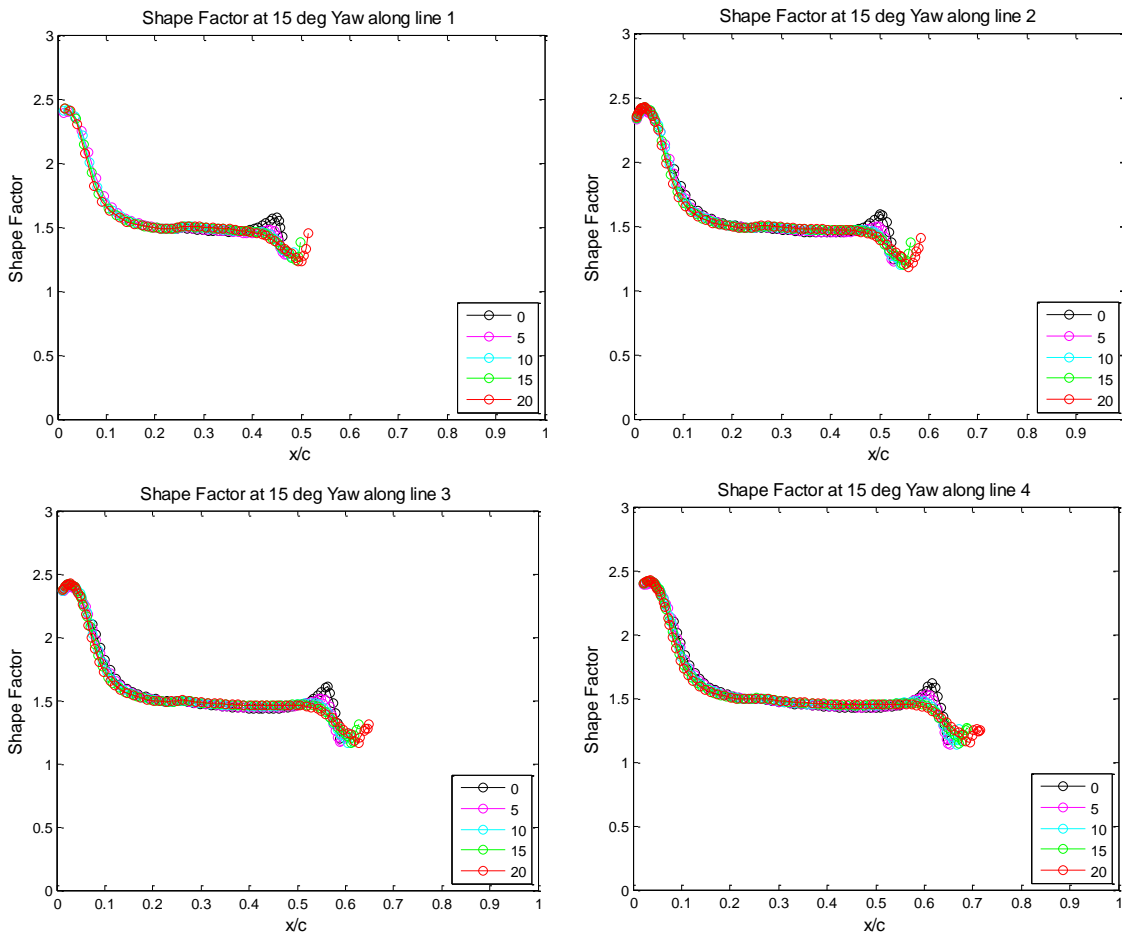
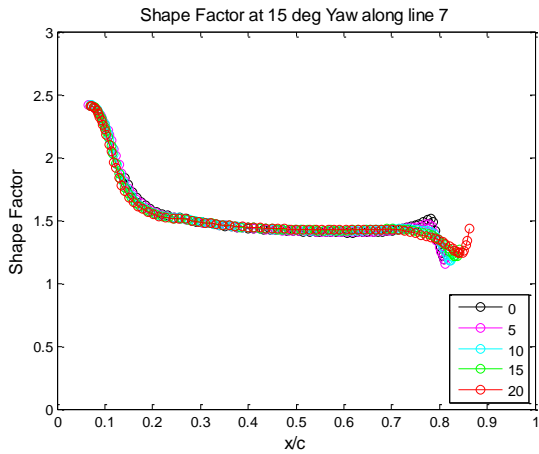
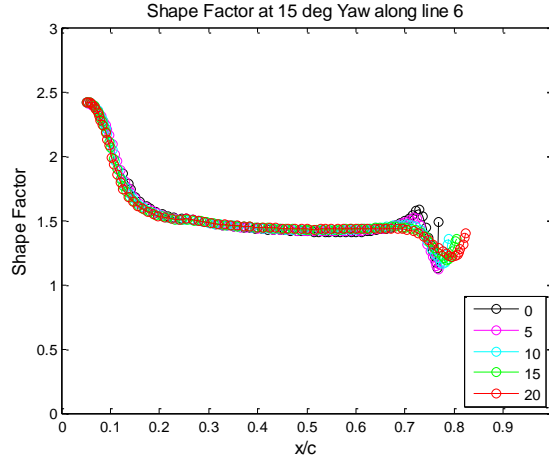
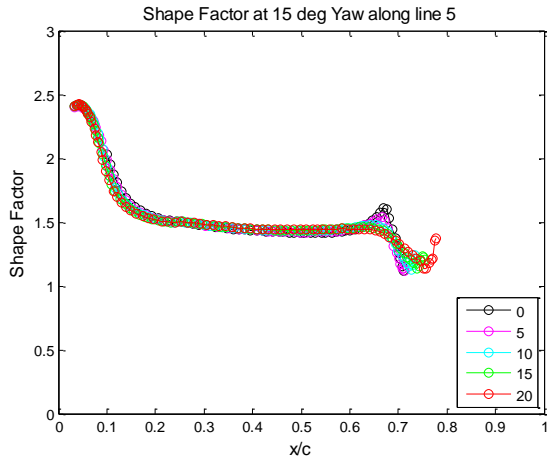


Figure 35 - Steady Momentum Thickness: 15° Yaw Turn, 0-20° Roll

Fifteen degree yaw case shape factors, Figure 36, show a minor impact of the forward change in curvature. Aft of the flow transition to turbulent, shape factors show minimal change along each characteristic line. Due to the correlation between the shape factor and the streamwise pressure gradient, this leads to the thought that changes in pressure gradient along the forward-mid section of the model are occurring primarily in the spanwise direction.





**Figure 36 - Steady Shape Factor:
15° Yaw Turn, 0-20° Roll**

In addition to the momentum thickness and shape factor, the edge velocities were established for the 15 degree yaw case and roll angles from 5 to 20 degrees. It can be seen that as roll angle increases, the bow's edge velocity also increases. Aft of $x/c \sim 0.1$, edge velocities remain fairly constant between roll angles.

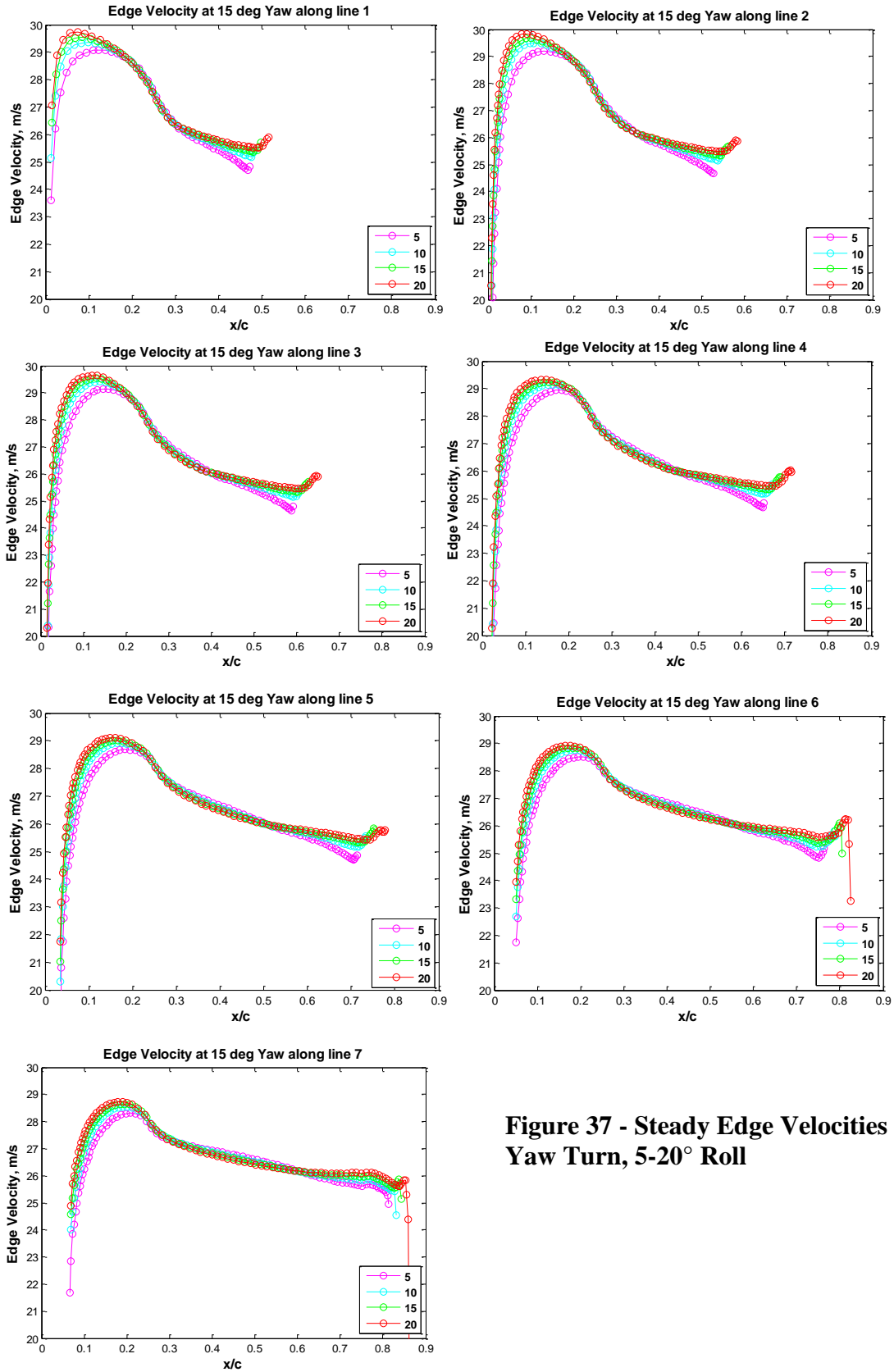


Figure 37 - Steady Edge Velocities 15° Yaw Turn, 5-20° Roll

D. Unsteady Forces and Moments

Unsteady forces and moments were simulated utilizing OVERFLOW's mesh motion capabilities. In this simulation, the Ellipsoid's angular velocity was specified as

$$\omega \equiv 2\pi f A \cos(2\pi f t) \quad (22)$$

where:

A = Amplitude (0.471 radians)

f = frequency (3 Hz)

t = time (seconds)

Time steps were established to ensure a maximum CFL value of 1^{16} . Sixty time step sub-iterations were used to allow the solution to converge to three to four orders of magnitude at each time step. Mentor's SST model was utilized based on its improved agreement with experimental data in steady conditions.

1. Unsteady Forces and Moments

Unsteady forces and moments for the 10 and 15 degree yaw cases are plotted against time and roll angle in Figures 38-41. The unsteady data are also plotted with steady data to show the simulated difference between the steady and unsteady forces and moments.

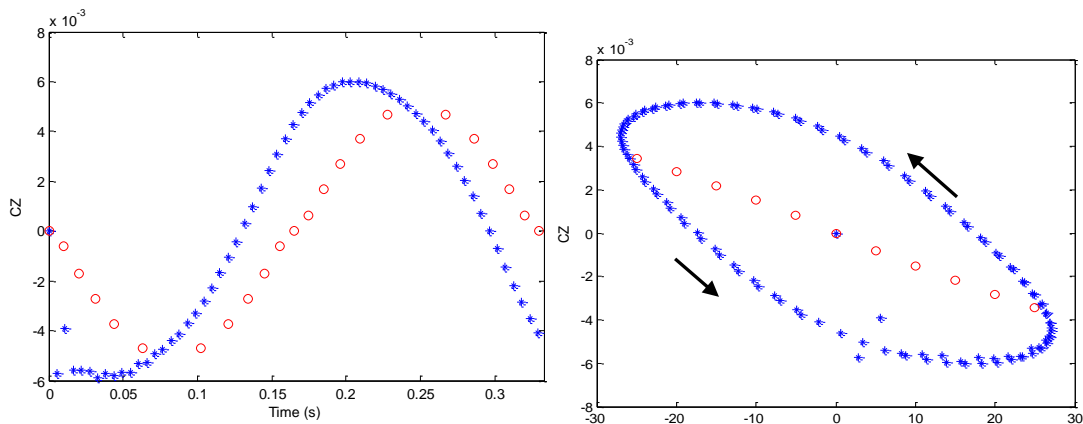


Figure 38 - Unsteady Normal Force Coefficients – 10° Yaw Turn

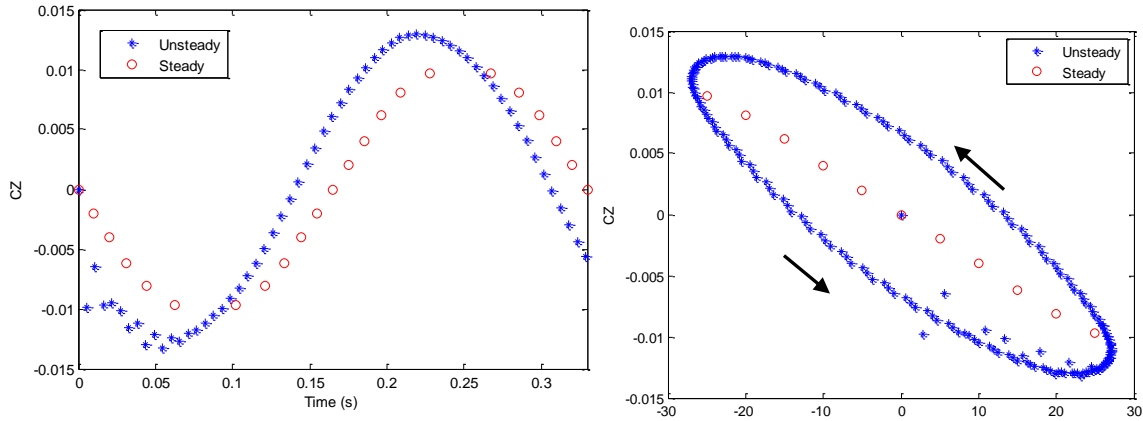


Figure 39 - Unsteady Normal Force Coefficients - 15° Yaw Turn

The simulated results of the unsteady normal force show a slight leading trend and increased amplitude with respect to the steady data. A large hysteresis loop is also seen to exist, highlighting the fully dynamic effect. The increased amplitude and hysteresis loop are both supported by the experimental data of Tanious¹⁴. Additional experimental data (currently being analyzed) also supports the leading shift calculated by the simulation. Discussion here will be limited to comparing trends between simulations and experimental data due to the additional data being analyzed at the time of this thesis' submission.

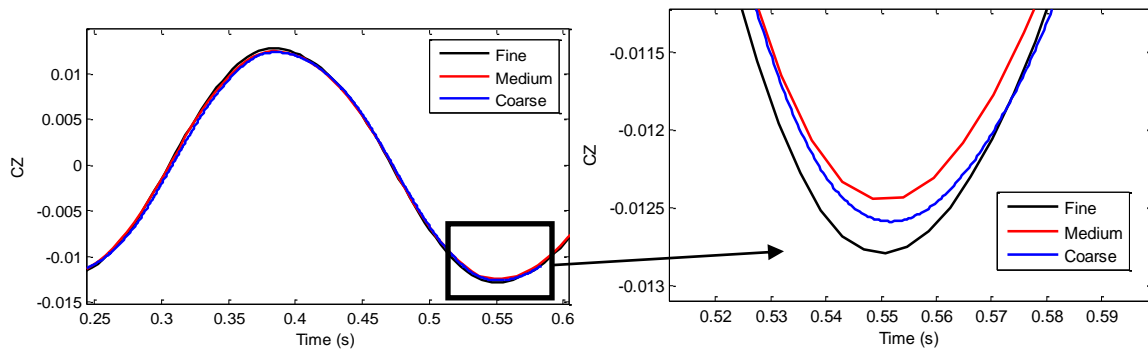


Figure 40 - Grid study of unsteady normal force coefficients – 15° Yaw Turn

Figure 40 plots unsteady normal forces of all three grid refinement levels. The fine mesh is seen to have slightly larger amplitude than the medium and coarse meshes. The amplitude, however, is not seen to converge as the solution delta grows and oscillates between the three grid levels.

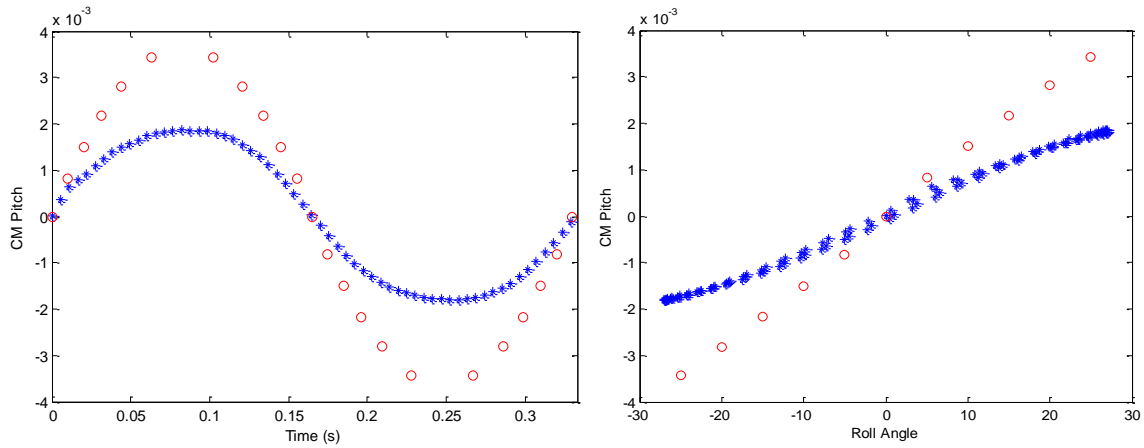


Figure 41 - Unsteady Pitching Moment Coefficients – 10° Yaw Turn

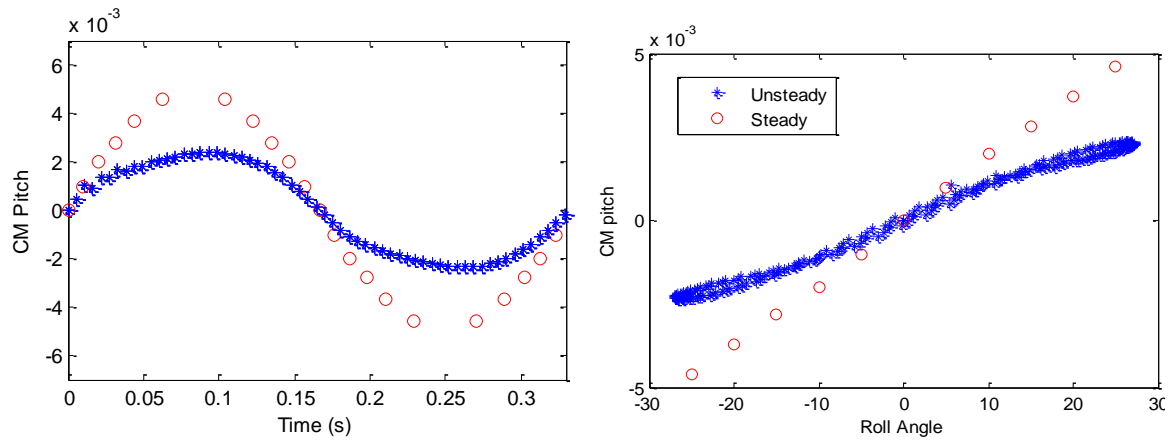


Figure 42 - Unsteady Pitching Moment Coefficients - 15° Yaw Turn

The pitching moment coefficient demonstrates a lag shift, which is in agreement with experimental data. The simulated amplitude, however, is reduced, where experimental data demonstrates equal amplitudes for steady and unsteady oscillations. The data also shows a full hysteresis loop, which is not replicated here. Small hysteresis loops are predicted at the peak angles, but not to the extent shown by the experiment.

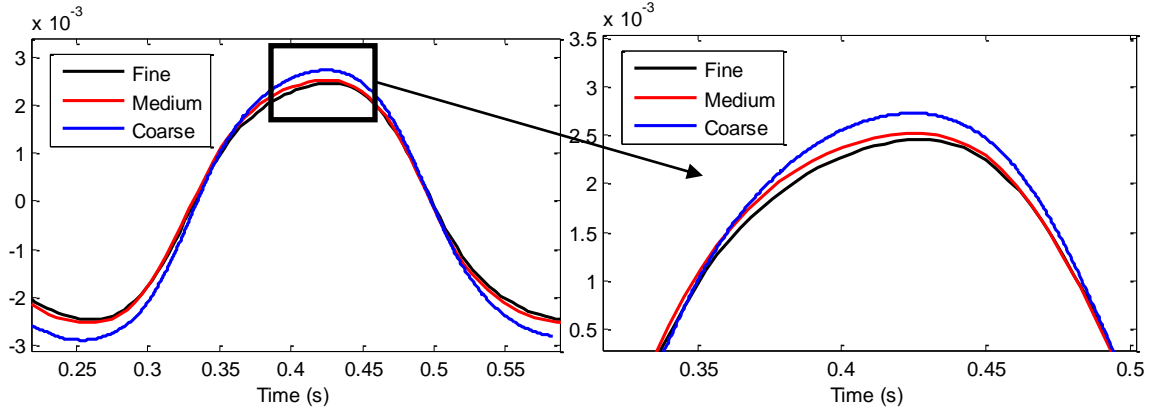


Figure 43 - Grid study of unsteady pitching moment coefficients – Spalart-Allmaras model

The pitching moment coefficient shows the solution moving towards grid convergence with increasing grid refinement as shown in Figure 43. It should still be noted, though, that there remains significant discrepancies between the unsteady simulations and experiment. Due to these discrepancies, no formal GCI is presented for these simulations.

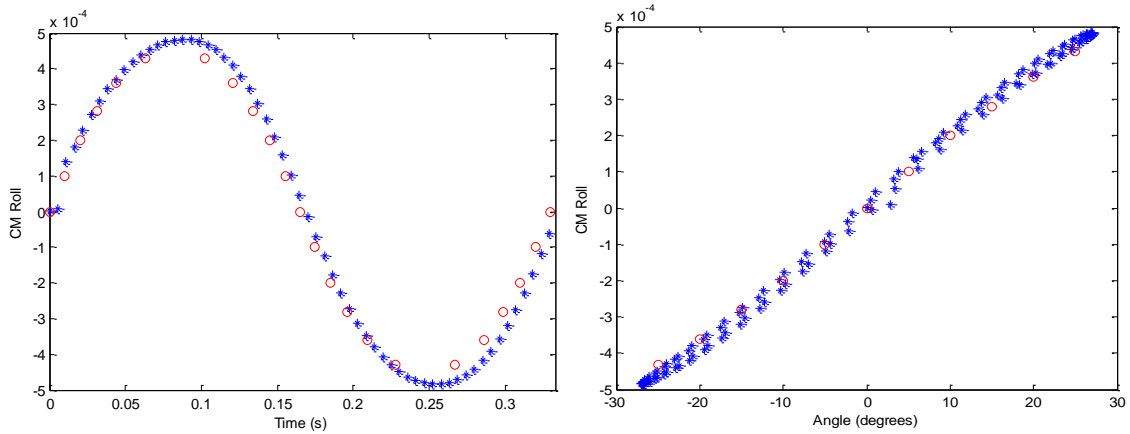


Figure 44 - Unsteady Rolling Moment Coefficients – 10° Yaw Turn

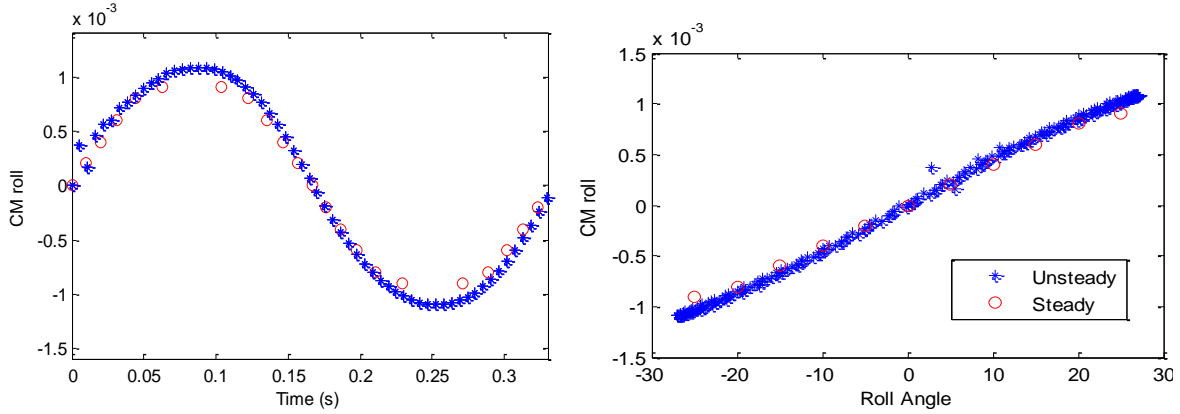


Figure 45 - Unsteady Rolling Moment Coefficients - 15° Yaw Turn

Unsteady roll moment simulations show an almost exact match between steady and unsteady values. Experimental data, however, shows the rolling moment tends to lead the steady data with increased amplitude.

2. Unsteady Separation

A study of crossflow separation trends lends insight to the unsteady forces and moments. Experimental results show hysteresis in the spanwise position of separation, as shown in Figure 46. Upsetting roll angles, 0 to 25 degrees, show separation is delayed compared to restoring angles, 25 to 0 degrees. Simulated separation, however, shows upsetting angles separating slightly further inboard than restoring angles.

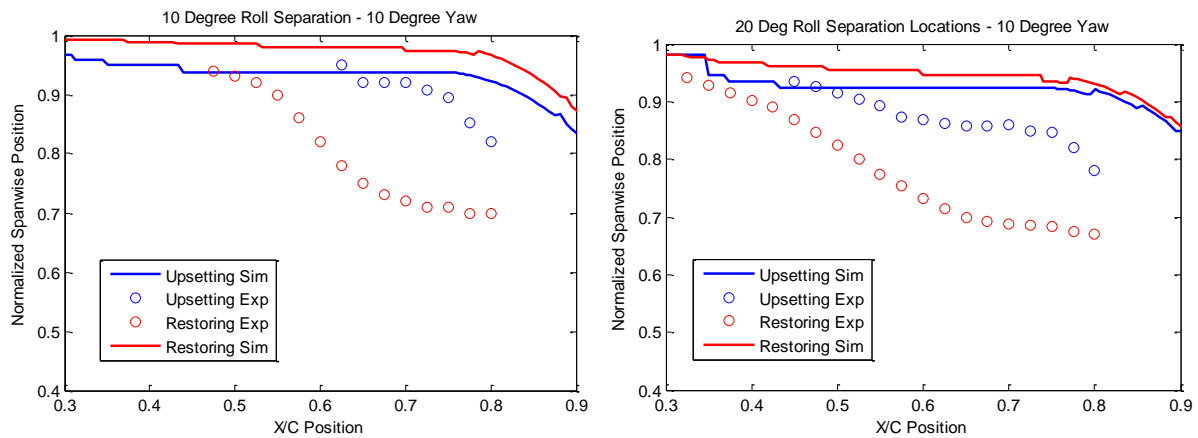


Figure 46 - Unsteady Separation Positions: 10° Yaw Turn

This trend appears to be a contributing source of the discrepancies in the unsteady forces and moments. As separation for steady simulations greater than 10 degrees showed the need for the

use of a model that more accurately models 3D flows, unsteady rolling simulations further supports the need for this type of analysis. The discrepancies between the unsteady simulations and the experiment should not, however, lead one to reject the viability of RANS as a concept design tool. Forces and moments for roll angles up to 10 degrees show good agreement with experimental data, allowing RANS to quickly provide reliable forcing results for a wide range of designs. The use of a hybrid RANS/LES model could then be used for detail analysis on a limited set of design concepts.

VI. Conclusions

Steady RANS does appear to be a viable tool for the predicting of non-BOR characteristics. Ahead drag coefficients agree with experimental data within 0.1% and pitched lift coefficients agree within 6%. Steady yaw turn forces and moments also show good agreement with experimental data up to roll angles of 10 degrees. Ahead skin friction calculations show improved agreement over LES w/wall functions and maneuvering separation calculations show good agreement up to roll angles of 10 degrees.

It is at 10 degrees roll that the impact of the change in curvature between the mid-body and elliptical ends was clearly seen in the pressure distributions and skin friction calculations. The discontinuity in surface curvature was shown to have a small influence; however the major source of the localized peaks in skin friction and pressure gradients is still unknown and warrants further research.

Until further research is conducted, designers are encouraged to avoid abrupt changes in curvature along the length of bodies. Further research needs to be performed establishing the change in curvature's impact on maneuvering forces and moments.

It is also recommended that further research be conducted into utilizing a fully boundary layer resolved hybrid RANS/LES model for detailed design analysis of maneuvering characteristics of angles greater than 10 degrees.

References

- [1] DeMoss, J.A., and Simpson, R.L., "A Study of the Boundary Layer Development, Skin Friction, and Wake on a non-Body of Revolution Ellipsoidal Model," *47th Aerospace Sciences Meeting*, AIAA-2009-1295, Orlando, FL, Jan. 5-8, 2009, pp. 1-30.
- [2] Granlund, K., and Simpson, R.L., "Experimentally Obtained Force and Moment Calculations on Steady and Unsteady Maneuvers of Slender Bodies," *47th Aerospace Sciences Meeting*, AIAA-2009-1292, Orlando, FL, Jan. 5-8, 2009
- [3] DeMoss, J.A., and Simpson, R.L., "Measurement of the Steady Skin Friction and Cross-Flow Separation Location on an Ellipsoidal Model in Yaw or Pitch over a Range of Roll Angles," *48th Aerospace Sciences Meeting*, AIAA-2010-317, Orlando, FL, Jan. 4-7, 2010, pp. 1-35
- [4] Bensow, R.E., "Large Eddy Simulation of the Flow Around a non-Body of Revolution Ellipsoidal Model at Steady Angles of Incidence and During Unsteady Motion," 2009. Chalmers University of Technology, Goteborg, Sweden.
- [5] Persson, T.M. Liefvendahl, Bensow, R. and Fureby, C., "Numerical Investigation of the Flow over an Axi-symmetric Hill using LES, DES, and RANS," *Journal of Turbulence*, 2005
- [6] Scott, N.W. and Duque, E., "Unsteady Reynolds-Averaged Navier-Stokes Calculation of the Flow Around a Prolate Spheroid," *4^{second} Aerospace Sciences Meeting and Exhibit*, AIAA-2004-55, Reno, NV, Jan. 5-8, 2004, pp. 1-11.
- [7] Menter, F.R., "Two-equation Eddy-viscosity Turbulence Models for Engineering Applications," *AIAA Journal* vol. 32 no.8, 1994, pp. 598-605
- [8] Rhee, S.H. and Hino, T., "Numerical Simulation of Unsteady Turbulent Flow Around Maneuvering Prolate Spheroid", *AIAA Journal*, Vol. 40, No. 10. October 2002, pp. 2017-2026.
- [9] Spalart, P.R. and Allmaras, S.R., "A One-equation Turbulence Model for Aerodynamic Flows," *29th Aerospace Sciences Meeting*, Reno NV, AIAA-92-0439, January 1992
- [10] Simpson, R.L., "Aspects of Turbulent Boundary-Layer Separation", *Prog. Aerospace Sci.* Vol. 32, 1996, pp. 457-521.
- [11] Lowe, K.T., and Simpson, R.L., "Turbulence structural measurements using a comprehensive laser-Doppler velocimeter in two- and three-dimensional turbulent boundary layers," *International Journal of Heat and Fluid Flow*. Vol. 29, 2008, pp. 820-829

- [12] Nichols, R.H. and Buning, P.G., "User's Manual for OVERFLOW 2.1," NASA, August, 2008.
- [13] Chan, W.M., Gomez, R.J., Rogers, S.E., and Buning, P.G., "Best Practices in Overset Grid Generation," *3rd AIAA Fluid Dynamics Conference*, AIAA-2002-3191, St. Louis, MS, June 24-26, 2002
- [14] Tanious, S, Granlund, K., and Simpson, R.L., "Unsteady Force and Moment Measurements on a non-Body of Revolution Vehicle Undergoing Oscillatory Roll," *48th Aerospace Sciences Meeting*, AIAA-2010-319, Orlando, FL, Jan. 4-7, 2010, pp. 1-12
- [15] Etkin, B., *Dynamics of Atmospheric Flight*, Dover Publications, 2005, Chap. 4.
- [16] Pandaya, S.A., Venkatswaran, S., and Pulliam, T.H., "Implementation of Preconditioned Dual-Time Procedures in OVERFLOW," *41st Aerospace Sciences Meeting and Exhibit*, AIAA-2003-72, Reno, NV, 2003, pp.1-12
- [17] Roache, P.J., "Verification of Codes and Calculations", *AIAA Journal* Vol. 36, No.5, May 1998, pp. 696-702.
- [18] Schetz, J.A., *Boundary Layer Analysis*. Prentice Hall. Upper Saddle River, NJ, 1993, Chap. 2.
- [19] Ludwig, H., and Tillmann, W., "Investigations of the Wall Shearing Stress in Turbulent Boundary Layers," *NACA TM 1285*, 1949
- [20] Hinze, J.O., *Turbulence, An Introduction to Its Mechanism and Theory*. McGraw-Hill Book Company, New York, 1959, Chap. 7.
- [21] Lighthill, M.J., *Part II of Laminar Boundary Layers*. Cambridge University Press. 1963
- [22] Knight, C.J. and Zajackowski, F.J., "Validation of a Viscous, Incompressible Throughflow Code", *33rd Aerospace Sciences Meeting and Exhibit*, AIAA 95-0864, Reno, NV, 1995
- [23] Wetzel, T.G. *Unsteady flow over a 6:1 prolate spheroid*, Ph.D Dissertation. Virginia Tech. 1996
- [24] Chang, P.K., *Separation of Flow*. Pergamon Press, Hungary, 1970, Chap. 1
- [25] OVERFLOW, NASA, Ver. 2.1w
- [26] MATLAB, The MathWorks, Inc., Ver. 7.7, 2008
- [27] FIELDVIEW, Intelligent Light, Ver. 12.3, 2010

Appendix A – Ellipsoid Database Generation Script - Matlab

```
%Geometry Inputs
Bow_length=0.4;
Mid_length = 0.8;
Mid_height = 0.231;
Mid_width = 0.4;
Stern_length=0.4;

%Grid Inputs
End_tightness = 10;
%End_tightness is used to concentrate nodes at the leading and trailing
%edges

theta=[0:0.5:180]';

%Mid-section
X_spacing = 0.1;
for m=1:Mid_length/X_spacing+1,
    for n=1:length(theta),
        x(n+length(theta)*(m-1))= Bow_length+(m-1)*X_spacing;
        y(n+length(theta)*(m-1))=(Mid_width/2)*cos(theta(n)*pi()/180);
        z(n+length(theta)*(m-1))=(Mid_height/2)*sin(theta(n)*pi()/180);
    end
end

%Stern Section
X_spacing = 0.002;
for a=1:Stern_length/(X_spacing/End_tightness)+1,
    for b=1:length(theta),
        stern_x(b+length(theta)*(a-1))=
Bow_length+Mid_length+Stern_length*(sin((pi/2)*(a-
1)/(Stern_length/(X_spacing/End_tightness)))));
        stern_y(b+length(theta)*(a-1))=real(sqrt(1-
(((stern_x(b+length(theta)*(a-1))-Bow_length-
Mid_length)^2)/Stern_length^2))*cos(theta(b)*pi()/180));
        if theta(b)< 180
            stern_z(b+length(theta)*(a-1))=real(sqrt(1-
(((stern_x(b+length(theta)*(a-1))-Bow_length-
Mid_length)^2)/(Stern_length^2))-(((stern_y(b+length(theta)*(a-
1)))^2)/(Mid_width/2)^2))*cos(theta(b)*pi()/180));
        else
            stern_z(b+length(theta)*(a-1))=-1*real(sqrt(1-
(((stern_x(b+length(theta)*(a-1))-Bow_length-
Mid_length)^2)/(Stern_length^2))-(((stern_y(b+length(theta)*(a-
1)))^2)/(Mid_width/2)^2))*sin(theta(b)*pi()/180));
        end
    end
end

%Bow Section
X_spacing = 0.002;
for a=1:Bow_length/(X_spacing/End_tightness)+1,
    for b=1:length(theta),
```

```

        bow_x(b+length(theta)*(a-1))=Bow_length*(1-cos((pi/2)*(a-
1)/(Bow_length/(X_spacing/End_tightness))));
    end
end

for c=1:a*b,
    bow_y(c)=stern_y(a*b+1-c);
    bow_z(c)=stern_z(a*b+1-c);
end

fid=fopen('Plot3D_Ellipsoid.txt','w');
fprintf(fid, '          3\n          %3g          %3g          1\n
%3g          %3g          1          %3g          %3g\n
1\n',b,a,n,m,b,a);
fprintf(fid, '% 10.9f % 10.9f % 10.9f',bow_x,bow_y,bow_z);
fprintf(fid, '\n % 10.9f % 10.9f % 10.9f',x,y,z);
fprintf(fid, '\n % 10.9f % 10.9f % 10.9f',stern_x,stern_y,stern_z);
fclose(fid);

```

Appendix B – Skin Friction Coefficient Script - FieldView

```
formula_restart_version: 1
normal
nrmlz(grad("Velocity Magnitude [PLOT3D]"))
du/dx
VecX(grad("u-velocity [PLOT3D]"))
du/dy
VecY(grad("u-velocity [PLOT3D]"))
du/dz
VecZ(grad("u-velocity [PLOT3D]"))
dv/dx
VecX(grad("v-velocity [PLOT3D]"))
dv/dy
VecY(grad("v-velocity [PLOT3D]"))
dv/dz
VecZ(grad("v-velocity [PLOT3D]"))
dw/dx
VecX(grad("w-velocity [PLOT3D]"))
dw/dy
VecY(grad("w-velocity [PLOT3D]"))
dw/dz
VecZ(grad("w-velocity [PLOT3D]"))
non_dim_X_wall_shear
("du/dx"*UnitX+"du/dy"*UnitY+"du/dz"*UnitZ) dot "normal"
non_dim_Y_wall_shear
("dv/dx"*UnitX+"dv/dy"*UnitY+"dv/dz"*UnitZ) dot "normal"
non_dim_Z_wall_shear
("dw/dx"*UnitX+"dw/dy"*UnitY+"dw/dz"*UnitZ) dot "normal"
Total_Shear
sqrt("non_dim_X_wall_shear"^2+"non_dim_Y_wall_shear"^2+"non_dim_Z_wall_shear"
^2)
Wall_Cf
("Total_Shear"* (342*1.65*e-5/1.6)) / (0.5*1.1*25.78125^2)
```